PKN2 regulates cell-junctions to limit colitis and colon tumour formation.

Jack C Henry[1], Ashley Campbell[1], Prerana Huddar[1], Joanne Sewell[1], Shinelle Menezes[1#], Adam Passman[2], Kane Smith[4], Shannah McGauran[1], Meng-Lay Lin[2], Ian Rosewell[3], Marnix Jansen[5], Neil McDonald[3], Trevor A Graham[4], Stuart McDonald[2] and Angus JM Cameron[1]*.

1. Kinase Biology Laboratory, Barts Cancer Institute, Queen Mary, University of London, John Vane Science Centre, Charterhouse Square, London, EC1M 6BQ, UK
2. Barts Cancer Institute, Queen Mary, University of London, John Vane Science Centre, Charterhouse Square, London EC1M 6BQ, UK
3. Francis Crick Institute, 1 Midland Road, London NW1 1AT, UK
4. Centre for Evolution and Cancer, Institute of Cancer Research, London, SM2 5NG, UK
5. University College London Cancer Institute, Huntley Street, London, WC1E 6AG, UK

* Corresponding Author: Angus JM Cameron. e-mail: a.cameron@qmul.ac.uk

Summary

Inflammation is a major driver of tumorigenesis and chronic colitis is a significant risk factor for developing colorectal cancer (CRC). Here, we identify the Rho regulated kinase PKN2 as a new tumour suppressor in colitis-associated CRC. Using conditional global and epithelial-specific knockout mice, we show that loss of PKN2 sensitises mice to inflammatory bowel injury and results in increased colorectal adenoma formation in a colitis-associated CRC model. Tumour burden tightly correlates with colitis disease severity suggesting elevated inflammatory tissue injury underlies tumour promotion in PKN2-targeted mice. Mechanistically, PKN2 localises to epithelial tight junctions and is required for maintaining effective barrier integrity in vivo, in intestinal organoids and in CRC cell models. We identify several candidate junctional substrates of PKN2 including S737 of the PP1 regulator ASPP2. These findings establish PKN2 as a functional regulator of gut barrier integrity encoded at genomic loci previously associated with bowel inflammation and tumour suppression in both humans and mice.

Introduction

Inflammatory bowel disease (IBD), comprising Crohn's disease and ulcerative colitis, is a group of chronic inflammatory disorders of the gastrointestinal tract, with a prevalence of approximately 0.3% in Western populations and a rising incidence in newly industrialized countries[1]. It is well established that patients with IBD have a significantly higher risk of developing colorectal cancer (CRC) compared to the general population and therefore often undergo regular colorectal screening tests to detect and remove pre-malignant lesions [2-4]. Chronic inflammation plays a central role in the development and progression of many cancers, including both sporadic and colitis-associated CRC. Supporting this, anti-inflammatory drugs such as Aspirin and COX inhibitors have been shown to significantly reduce the risk of developing sporadic CRC [5-8]. In experimental models, disrupting inflammatory pathways, both intrinsic to epithelial cells and through immune cell targeting, dramatically reduces tumour formation in both the azoxymethane/dextran sodium sulphate (AOM/DSS) and genetic APC-targeting models[9-12].

Given the strong link between inflammation and colorectal cancer risk, there has been considerable interest in identifying genetic loci that predispose individuals to IBD. Chromosome arm 1p has been identified as a significant susceptibility locus for human IBD; however, it contains over a thousand genes, making it difficult to pinpoint key candidates. [13]. Two potential candidates on 1p36 include TNF receptor and Caspase 9, yet other candidates on 1p are yet to be discovered [14,15]. Genetic mouse studies have tried to further elucidate some of the key regions on chromosome 1p by exploring differential sensitivity in different background strains. *Cdcs1 (cytokine deficiency-induced colitis susceptibility-1)* on chromosome 3 is a locus containing 340 genes, syntenic with human 1p. Cdcs1 is well characterised as the cause of increased susceptibility between BALB/c, C3H/HeJBir or C3H/HeN and C57BL/6J strains in T-bet($^{-/-}$).Rag2($^{-/-}$)[16], Il10($^{-/-}$)[17,18] or Gnai2($^{-/-}$)[19] knockout colitis models respectively. Further research has identified the overlapping (colitis associated) colon cancer susceptibility locus also on mouse chromosome 3 (CCs3). This locus was identified to be the cause of the increased susceptibility to AOM/DSS induced colorectal tumours experienced by the A/J mouse strain when compared to the relatively resistant C57BL/6J [20].

Here, we identify PKN2 as a key gene on human chromosome 1p, syntenic with murine *Cdcs1* and CCs3, that confers susceptibility to colitis and functions as a tumour suppressor in colitis-associated colorectal cancer (CA-CRC). Global or epithelial-specific loss of PKN2 in vivo sensitises mice to DSS-induced colonic injury and promotes colorectal adenoma formation. PKN2 deficiency disrupts epithelial tight junction integrity in vitro and in vivo, resulting in increased barrier permeability and impaired tissue repair. Tight junction repair depends on the kinase activity of PKN2, which phosphorylates key substrates including the non-redundant target ASPP2. ASPP2 in complex with PP1 enables dephosphorylation of ZO-1 and other junctional proteins, which is critical for tight-junction repair and stability. These findings establish PKN2 as a critical regulator linking epithelial barrier integrity to inflammatory and tumour-suppressive processes, providing new mechanistic insight into the molecular basis of colitis-associated colorectal cancer.

Results

PKN2 loss promotes colitis and colitis -associated colorectal cancer

To test if PKN2 can act as a colitis-associated tumour suppressor, we exploited our inducible conditional PKN2 knockout mouse (global-iPKN2^{KO}: *Pkn2$^{fl/fl}$;Rosa26-CreER^{T2}*) and the two stage azoxymethane (AOM)/Dextran sodium-sulphate (DSS) colitis-associated colorectal tumour induction model (Figure 1A). Global PKN2^{KO} is embryonic lethal[21], but inducible conditional deletion in adults is generally well-tolerated[21,22] with minimal macroscopic effects on normal colon homeostasis. Five consecutive days of treatment with tamoxifen in the iPKN2 model was sufficient to activate Cre and induce loss of PKN2 DNA and protein in the intestines of adult mice (Figure S1A, B) [21]. To induce tumours, WT and PKN2 targeted mice were treated with a single dose of the mutagen AOM (10mg/kg) followed by three repeated rounds of 1% DSS, which typically results in tumour formation at 90 days, mimicking the development of human colitis associated colorectal cancer [23]. Typically, DSS is administered at 2-2.5% in C57BL/6 mice but pilot experiments indicated that PKN2 targeted mice tolerated 2% DSS regimens poorly, exhibiting exacerbated weight loss, poorer general condition (scored 1-3) and increased disease activity (Figure S1C-E). Even at the reduced dose of 1% DSS, experimental cohorts were subject to some attrition, where both heterozygous (global-iPKN2^{HET}) and homozygous PKN2 (global-iPKN2^{KO}) deletion significantly exacerbated weight loss, disease activity and survival (scored 1-14) [24] (Figure 1B-G). Surviving mice with PKN2 loss continued to show increased weight loss and disease activity across the experimental time course (Figure S1F-I). At 90-days post-AOM mice were examined for tumour induction which revealed an increase in macroscopically visible tumour incidence, multiplicity and tumour burden in PKN2-targeted mice

(Figure 1H-K). No tumours were observed at 90 days in cohorts treated with AOM alone. Pathological analysis identified that global-iPKN2^{KO} bowels presented with more high-grade tubular adenomas while incidence of low-grade tissue dysplasia and tumour size distribution was similar between genotypes (Figure S1J-L). Globally targeting PKN2 did not induce polydipsia or alter relative DSS dose (Figure S1M). PKN2 targeted mice also presented with splenomegaly (Figure S1N, O) but had no change in colon length or overt pathology associated with other organs (Figure S1P). We conclude that haploinsufficiency of PKN2 is sufficient to exacerbate DSS induced disease and CRC adenoma formation, and that homozygous loss induces a more penetrant phenotype.

We sought to characterize the adenomas to identify phenotypes associated with PKN2 loss. Immunohistochemical analysis of immune cell markers and ki67 expression identified no obvious differences in immune cell infiltrate or proliferation between genotypes (Figure S2A-E). To further explore the phenotypes of PKN2 loss in colitis associated adenomas we performed Smart-3SEQ transcriptomics[25] on a selection of laser captured epithelial regions for each genotype. Importantly, PKN2 expression is significantly reduced in heterozygous and homozygous knockouts of PKN2 (Figure S2F). However, principal component analysis identifies largely overlapping clustering between genotypes (Figure 1L), reflecting a random varied tumour population in which PKN2 status does not consistently dictate selected tumour phenotypes. In addition, gene set enrichment analysis between wild-type and global-iPKN2^{KO} adenomas does not identify any clear increase to cancer hallmarks or oncogenic signalling pathway activity including APC/WNT, RAS, TP53 and YAP (Figure S2G, H). One of the most significant negatively enriched gene sets are genes upregulated by a constitutively active (Q63L) form of RHOA, a regulator of PKN2 [26]. Interestingly, six pathways were also significantly enriched in KO adenomas from the mouse tumour phenotypes ontology collection of gene sets including tumour incidence by chemical induction, tumour growth size and metastatic potential, suggesting PKN2 might antagonise the expression of pro-tumorigenic genes this model (Figure 1M, N, S4I). In summary, the increase in high-grade dysplasia incidence, overlapping principal components, and a tight correlation between tumour burden and average disease activity (Figure 1O) suggests PKN2 loss primarily promotes colitis-associated colorectal cancer not through an oncogenic program, but by exacerbating an environment that promotes neoplastic initiation.

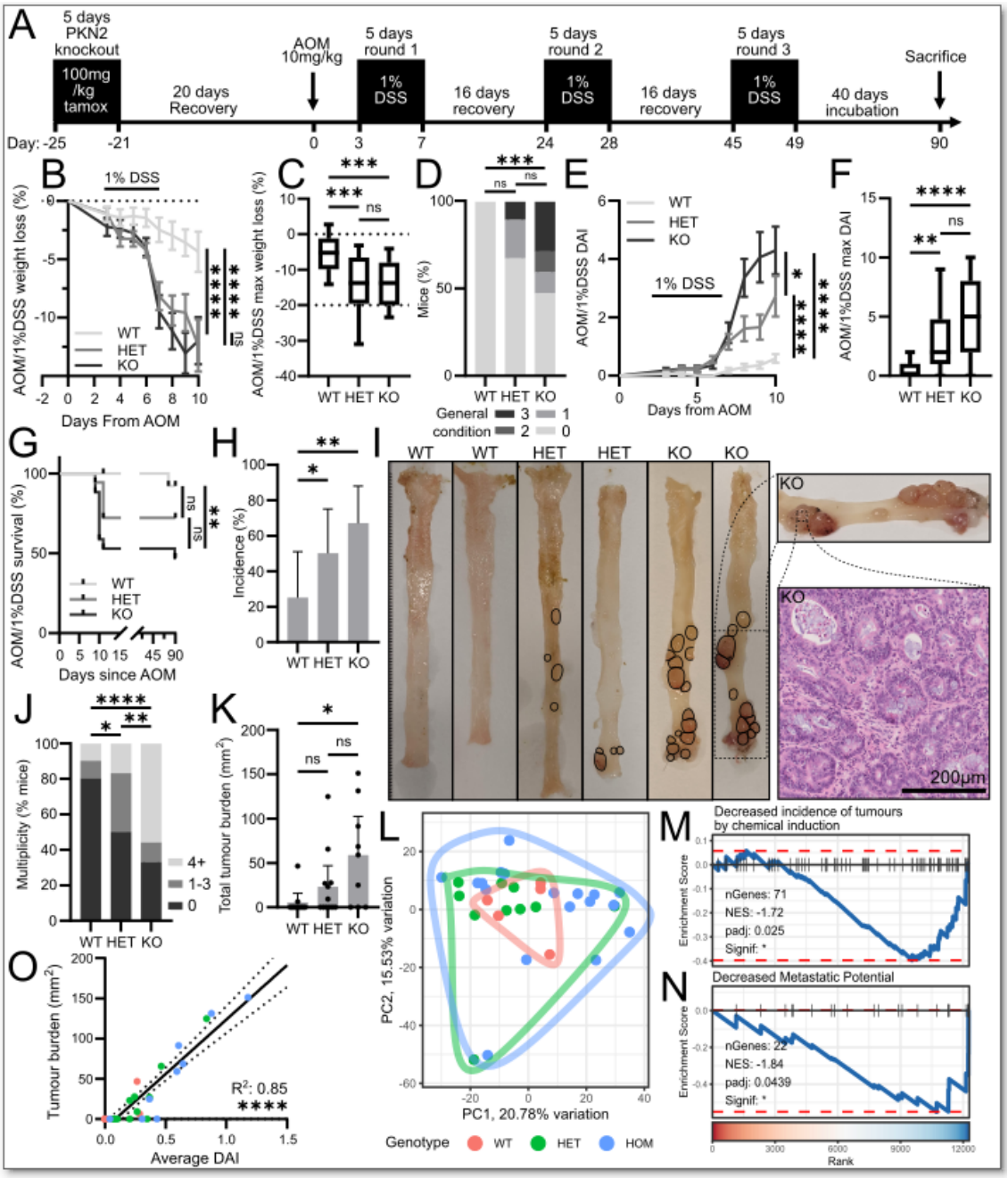

Figure 1: PKN2 loss sensitises mice to AOM/DSS treatment and promotes colitis-associated colorectal cancer. A) Outline of the AOM/1%DSS treatment protocol in PKN2 KO mice. **B, C)** Average (B) and maximum (C) weight change in response to the first 10 days of AOM/DSS treatment (WT: n=17, HET: n=18, KO: n=17). Statistical significance was determined using a two-way repeated measures ANOVA (B) and Tukey's multiple comparisons test (C). **D)** General condition scored 0-3 per mouse in response to the first 10 days of AOM/DSS treatment (WT: n=17, HET: n=18, KO: n=17). Statistical significance was determined using a Dunnett's multiple comparisons test. **E, F)** Average (E) and maximum (F) disease activity index (DAI) per mouse in response to the first 10 days of AOM/DSS treatment (WT: n=17, HET: n=18, KO: n=17). Statistical significance was determined using a two-way repeated measures ANOVA (E) and Tukey's multiple comparisons test (F). **G)** Kaplan Meier plot

describing the survival of mice in response to the AOM/DSS treatment protocol. Statistical significance was determined using a Log-rank test. **H)** Incidence of surviving mice at a 90-day fixed timepoint (WT: n=10, HET: n=12, KO: n=9). Statistical significance was determined using a Chi-square test. **I)** Representative images of fresh colons following the AOM1%DSS model. Region of expanded KO tumour pathology is shown. **J, K)** Multiplicity (J) and tumour burden (K) of surviving mice at a 90-day fixed timepoint (WT: n=10, HET: n=12, KO: n=9). Statistical significance was determined using a Chi-square test. **L)** Principal component analysis of Smart3-Sequenced epithelial samples laser captured from FFPE sections (WT: n=5, HET: n=10, KO: n=18). **M, N)** Gene set enrichment analysis on ranks from differential expression analysis of KO vs WT adenomas using the mouse tumour phenotypes ontology collection of gene sets. **O)** Correlation of tumour burden and average disease activity (WT: n=10, HET: n=12, KO: n=9). Mouse genotype is coloured the same as in panel L.

PKN2 loss aggravates inflammatory bowel injury

To characterise the sensitisation of mice to DSS induced bowel injury we first examined the impact of PKN2 loss on acute DSS treatment. Bowels harvested 8-days post initiation of 1% DSS treatment presented regions of epithelial erosion, exudate, goblet cell depletion and crypt damage with the most severe phenotypes associated with PKN2 loss (Figure 2A-E).

Single cell RNA sequencing studies of normal and Crohn's disease inflamed human colon identify PKN2 expression is enriched in, but not restricted to, epithelial cells (Figure S3A, B). To explore if sensitisation to inflammatory bowel injury reflects an epithelial specific role for PKN2, the floxed PKN2 mouse was crossed onto the Villin-Cre (*Pkn2*$^{fl/fl}$*;Vil1-CreER*^{T2}) specific driver allowing for intestinal epithelial specific knockout of PKN2 (Epi-iPKN2^{KO}). PCRs of isolated epithelial crypts two weeks following tamoxifen treatment identify strong recombination and PKN2 knockout in the epithelial compartment of epi-iPKN2^{KO} mice (Figure S3C). Following a 2% DSS treatment regime without AOM, PKN2 KO mice show a similar sensitisation to the global-PKN2 KO, with exacerbated weight loss and DAI scores (Figure 2F, G). Bowel tissue harvested 8-days post 2% DSS treatment also presented with a significant decrease in total colon length (Figure S3D) but no change to spleen size (Figure S3E). Histologically mice with epithelial specific PKN2 loss also had an increased prevalence of erosions, crypt loss and depletion of goblet cells (Figure 2H, 2I, S3F, S3G), highlighting that PKN2 loss in the epithelial compartment is sufficient to aggravate inflammatory bowel injury.

Erosions were primarily localised to distal regions in all genotypes. On average, distal submucosae showed increased thickness in global and epi-iPKN2^{KO} mice with higher levels of cellularity and CD45+ immune cell infiltrate (Figure 2J-L, S3H-L). Surrounding distal crypts also contained more CD45+ immune cell infiltrate indicating heightened local inflammation (Figure S3M, N).

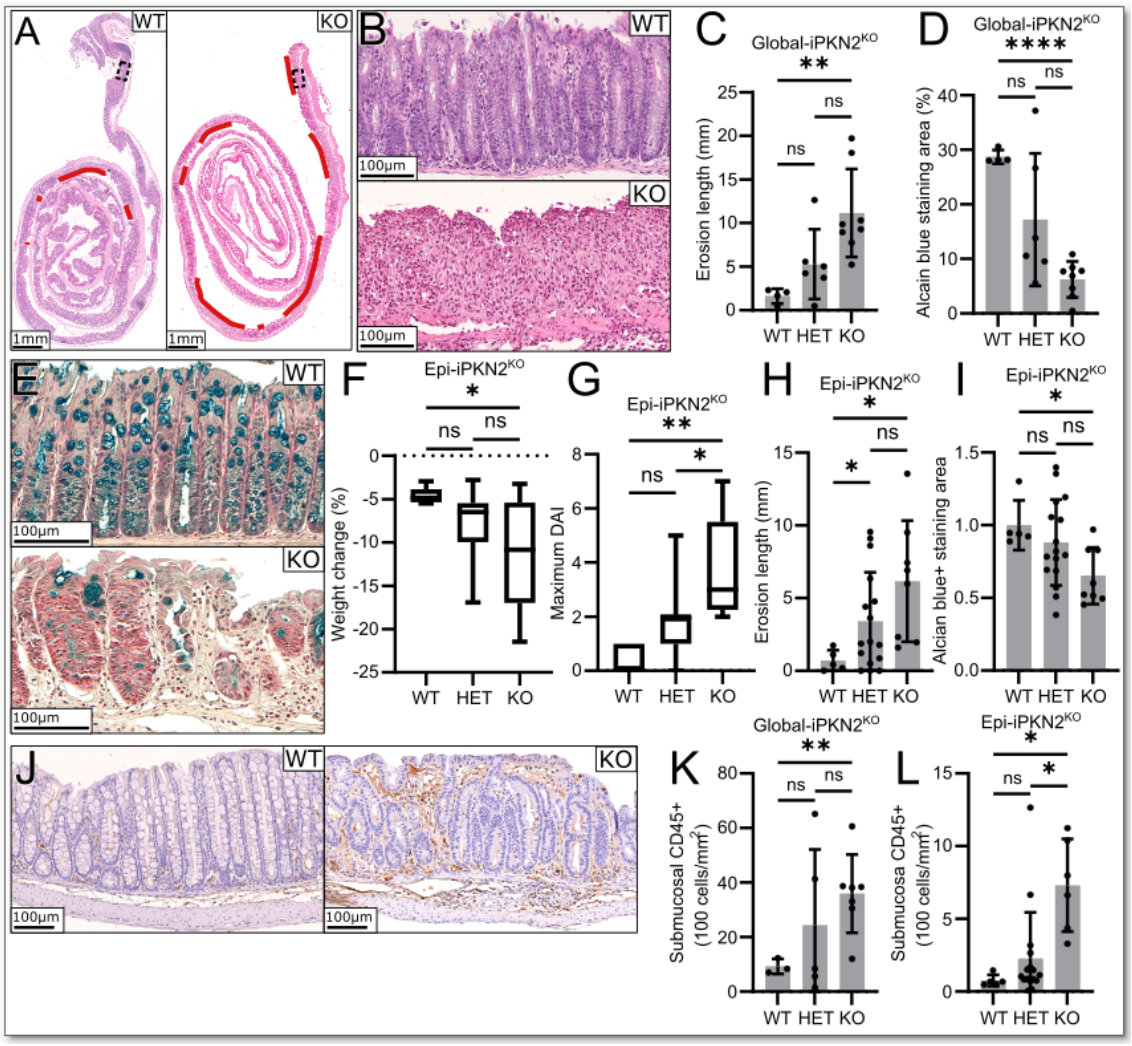

Figure 2: PKN2 loss aggravates inflammatory bowel injury. A-C) Degree of epithelial erosion in mice 8 days following initiation of AOM/1%DSS treatment in global-iPKN2^{KO} mice (WT: n=4, HET: n=6, KO: n=8). Statistical significance was determined using a Dunnett's multiple comparisons test. Erosions are indicated with a red line and zoomed portion in B is outlined in A with a dashed rectangle. **D, E)** Goblet cell depletion indicated by alcian blue staining decrease in response to AOM/1%DSS treatment in global-iPKN2^{KO} mice (WT: n=4, HET: n=6, KO: n=8). Statistical significance was determined using a Dunnett's multiple comparisons test. **F, G)** Maximum weight loss and disease activity index (DAI) in response to the first 10 days of AOM/1%DSS treatment in epi-iPKN2^{KO} mice (WT: n=5, HET: n=16, KO: n=8). Statistical significance was determined using a Tukey's multiple comparisons test. **H, I)** Erosion length (H) and goblet cell depletion indicated by alcian blue staining (I) in response to 2%DSS treatment in epi-iPKN2^{KO} mice (WT: n=5, HET: n=16, KO: n=8). Statistical significance was determined using a Dunnett's multiple comparisons test. **J-L)** CD45+ immune cell infiltration into distal submucosa in global-iPKN2^{KO} in response to AOM/1% DSS treatment (J, K) and epi-iPKN2^{KO} mice in response to 2%DSS treatment (L). Statistical significance was determined using a Dunnett's multiple comparisons test (K: WT: n=3, HET: n=5 KO: n=7, L: WT: n=5, HET: n=16, KO: n=6,).

PKN2 loss sensitises intestinal epithelial tight junctions

The observation that epithelial PKN2 deletion in vivo led to more tissue damage prompted us to investigate a role for PKN2 in epithelial junction formation. PKN2 has been shown to associate with

and regulate apical junction maturation in bronchial epithelial cells[27]. More recently, a study in MDCK-II cells also localised PKN2 to apical junctions as part of the Crumbs complex[28]. Staining of PKN2 in DLD1 and Caco2 colorectal cancer cell lines show that PKN2 localises to zona occludens-1 (ZO-1) positive tight junctions (Figure S4A, B).

As DSS induced tissue damage has been directly associated with ZO-1 loss at the epithelial barrier[29], we hypothesised PKN2 loss may exacerbate epithelial junction breakdown. Tissue staining for the tight junctional protein ZO-1 in colon sections 8 days post DSS treatment showed a loss of staining area in global and epithelial-specific PKN2 KO mice (Figure 3A-C). A reduction in ZO-1 staining was also present in non-DSS treated mice two weeks following PKN2 knockout (Figure S4C) but less obvious 15-days following DSS treatment (Figure S4D).

To further investigate epithelial barrier integrity in vitro, colonic epithelial organoids were generated from wild-type C57BL/6 and *Pkn2*$^{fl/fl}$*;Rosa26-CreER*^{T2} mice, allowing for the in vitro knockout of PKN2 with 4-hydroxytamoxifen (TAM) treatment (Figure S4E). Staining of organoids adhered to coverslips confirms PKN2 is also localised to apical junctions with ZO-1 in primary colonic epithelial cells (Figure 3D). Knockout of PKN2 in vitro reduced ZO-1 positive junction formation in intact organoid cultures (Figure 3E, F). Both junctional ZO-1 staining intensity and junctional area were further reduced in organoids without PKN2 following treatment with 10µg/ml DSS (Figure 3G). While DSS treatment also reduced wild-type organoid junctional area and intensity, no difference was detected in response to 4-hydroxytamoxifen (TAM, Figure S4F-H).

We also explored a tight junction role for PKN2 in DLD1 CRC cells. Knockdown of PKN2 using siRNA, or knockout with CRISPR-Cas9 PKN2 targeting, both disrupted ZO-1 positive tight junction formation in DLD1 cells (Figure 3H, I, S4I-N). CRISPR knockout of PKN2 had minimal effects on adherens junctions in DLD1 cells (Figure S5A). Using the Flp-In T-Rex inducible cell line system (Invitrogen), we produced stable DLD1 cell lines that overexpress wild-type (iDLD1 WT-PKN2) or kinase dead PKN2 (iDLD1 KD-PKN2 D782A) following tetracycline. Overexpression of KD-PKN2 in iDLD1 cells has a dominant negative effect on junction formation, demonstrating that PKN2 kinase activity is essential for the function of PKN2 in tight junction formation (Figure S5B-E). Overexpression of WT-PKN2 in iDLD1 cells had little effect on ZO-1 positive tight junction formation (Figure S5F-I).

Tight junctions in colonic epithelia are essential for preventing the influx of luminal pathogens and toxins into the mucosa [30]. Functional Transwell™ assays demonstrate PKN2 knockout increases DLD1 epithelial monolayer barrier permeability to fluorescent 40kda FITC-dextran without influencing cell viability (Figure 3J; S5J). Furthermore, treatment of cell monolayers with 50 mg/ml DSS more potently sensitises PKN2 knockout junctions to dextran permeability compared to wild-type controls, while having a minimal impact on cell viability (Figure 3K, S5K).

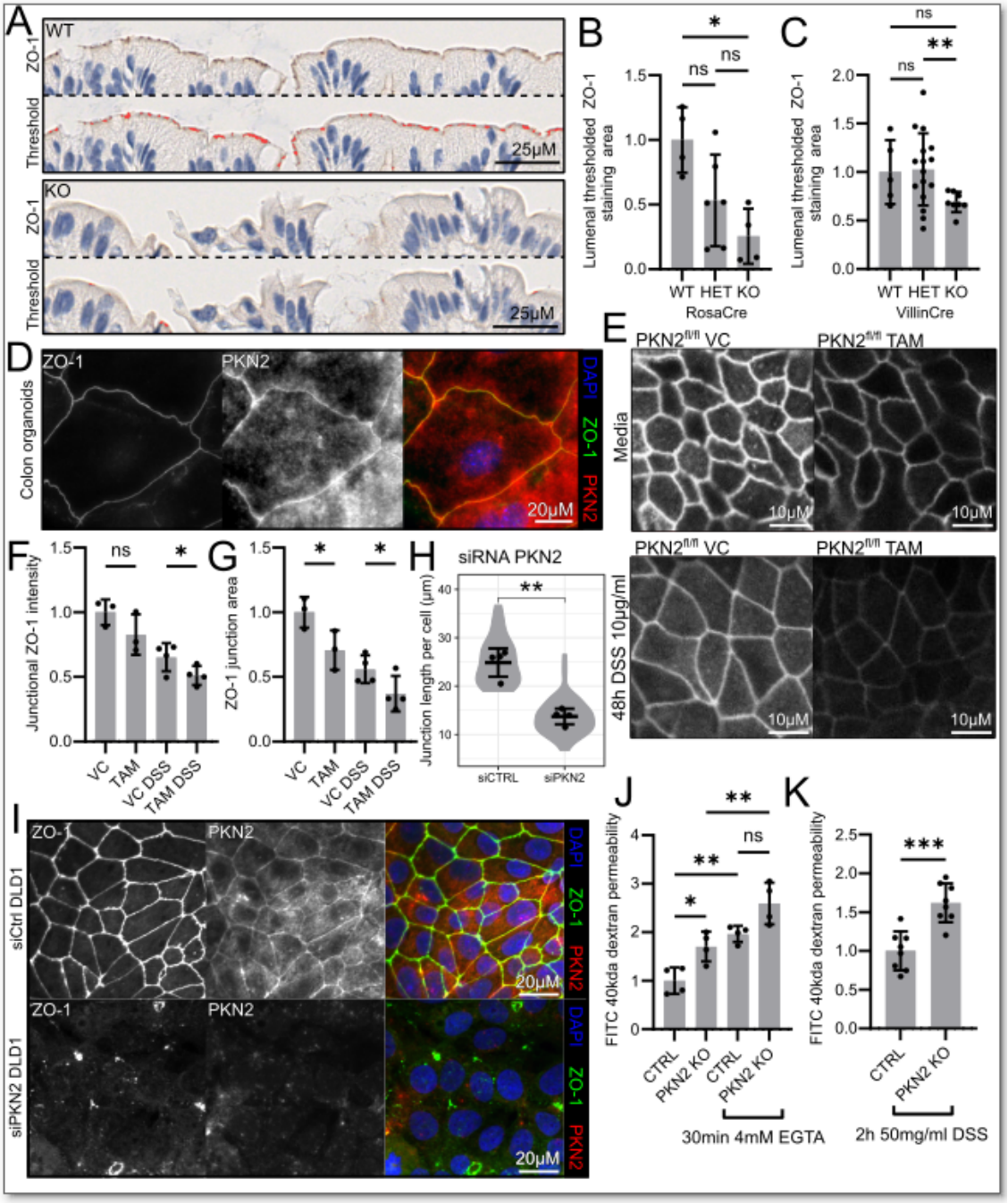

Figure 3: PKN2 loss sensitises intestinal epithelial tight junctions to DSS treatment. A-C) Immunohistochemical analysis of distal colonic luminal epithelial ZO-1 staining in mice 8 days after initiation of 5 days of 1% DSS treatment in global-iPKN2^{KO} (A, B) and epithelial-iPKN2^{KO} (C) mice. Pixel threshold DAB staining intensity shown bottom. Statistical significance was determined using a Holm-Šídák's multiple comparisons test (B: WT: n=4, HET: n=6, KO: n=4, C: WT: n=5, HET: n=, KO: n=8 n = 29). **D)** Staining of PKN2 and ZO-1 in C57BL6 colonic organoids grown in 2D. **E-G)** Staining of ZO-1 in primary mouse Rosa$^{Cre/+}$/PKN2$^{fl/fl}$ organoids grown in 3D following 48h treatment with vehicle control or 10µg/ml DSS. Graphs demonstrate a loss of junctional ZO-1 staining intensity (F) and area (G)

following PKN2 knockout with 4-OHT treatment (TAM). Statistical significance was determined using a Holm-Šídák's multiple comparisons test (n=3). **H-I)** Loss of ZO-1 positive tight junction formation following PKN2 knockdown with a PKN2-targeting siRNA pool. Tight junction loss was quantified by average length of junctional ZO-1 per cell. Statistical significance was determined using an unpaired, two-tailed t-test (n=4) **J)** 40kda FITC dextran permeability through an epithelial monolayer of PKN2 knockout CRISPR cells compared to a CRISPR control gRNA line seeded onto 0.4µM transwells. 4mM EGTA was added for 30mins to disrupt tight junctions. Statistical significance was determined using a Tukey's multiple comparison test (n=4). **K)** 40kda FITC dextran permeability through an epithelial monolayer of PKN2 knockout CRISPR cells compared to a CRISPR control gRNA line seeded onto 0.4µM transwells and treated with 50mg/ml DSS

Transcriptomic consequences of PKN2 loss reveal links to human colitis and junctional integrity

To further understand how PKN2 loss alters cellular behaviour we performed RNA sequencing experiments on PKN2 knockout organoids and PKN2-siRNA DLD1 cells. Principle component analysis of PKN2 knockout organoids and PKN2 knockdown in DLD1 cells identifies tight clustering of biological repeats with PKN2 loss driving the principal component with the highest degree of variance (Figure 4A; Figure S6A). PKN2 is the most significantly differentially expressed gene in organoid RNA sequencing analysis and the second most in siRNA DLD1 cells, indicating penetrant targeting of PKN2 (Figure 4B, Figure S6B). Hallmark gene set enrichment analysis (GSEA) identifies a significant enrichment to inflammatory response genes and TNFα signalling suggesting that PKN2 loss promotes organoid intrinsic inflammatory signalling (Figure S6C). PKN2 also regulates the expression of several known cancer genes (Figure 4C) (Cancer Gene Consensus - COSMIC).

To assess the ability of PKN2 loss to mimic human colitis we compared transcriptional profiles between PKN2 knockout organoids and human organoids isolated from patients with colitis [31]. These organoids have large degree of overlap in hallmark GSEA suggesting that PKN2 loss is indicative of human disease (Figure 4C). Moreover, PrismEXP predictions from the ARCHS4 database containing vastly integrated RNA sequencing data predict PKN2 has roles in rectal prolapse, hematochezia and colon cancer in human and mouse phenotype annotations (Figure S6D, E); all these phenotypes are exacerbated in our PKN2 specific mouse models. PKN2 also has predicted roles in cell junctions, transcriptional regulation and the YAP pathway (Figure S6F).

Next, we hypothesised that PKN2 loss may impact on tight junction formation through the regulation of the transcriptome. Analysis of gene sets associated with cell junctions identifies a general upregulation to genes involved in junction production in PKN2 KO organoids, PKN2-siRNA treated cancer cells and human colitis organoids (Figure 4E, S6G). The fact that junction genes are generally upregulated in response to PKN2 loss or in human colitis may imply a compensatory rather than mechanistic role, where increased expression of junction proteins may occur as a feedback response to loss of junctional integrity. Furthermore, analysis of PKN2-low colon (COAD) and rectal (READ) adenocarcinoma in TCGA data also identifies a significant enrichment in apical junction genes suggesting that this mechanism may also be relevant to sporadic colorectal cancer (Figure S6H, I).

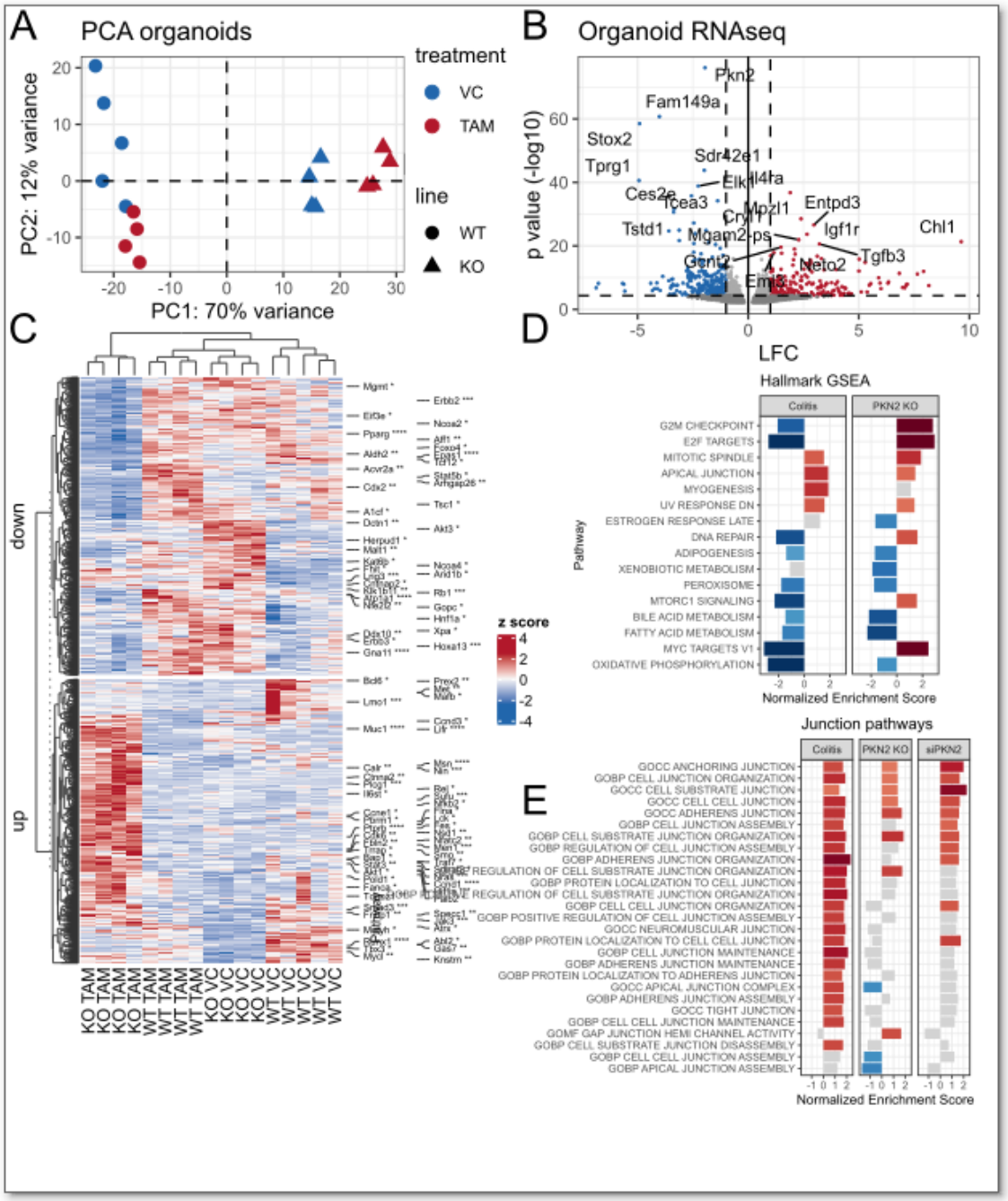

Figure 4: Transcriptomic profiling of PKN2 loss reveals inflammatory and junctional pathway modulation. A) Principal component analysis of RNA sequencing data from wild-type and Rosa$^{Cre/+}$/PKN2$^{fl/fl}$ primary mouse colon organoids treated with 4-OHT tamoxifen or a vehicle control. **B)** Differential gene expression analysis identifying the most significantly differentially expressed genes between vehicle control and tamoxifen treated PKN2-KO organoids, accounting for the effects of tamoxifen treatment on wild-type organoids. **C)** Significant differentially expressed genes between vehicle control and tamoxifen treated PKN2-KO organoids, accounting for the effects of tamoxifen treatment on wild-type organoids. Known cancer genes from the Cancer Gene Consensus are labelled. **D)** Hallmark gene set enrichment analysis comparing the response of PKN2 KO in primary

mouse organoids and change in expression in organoids from patients with colitis. **E)** Upregulation in pathways from the GO collection of gene sets related to junction formation and regulation.

PKN2 mediated regulation of junction components.

Since PKN2 kinase activity is important for junction formation and PKN2 colocalises with apical junction proteins, we hypothesised that PKN2 may directly phosphorylate and regulate junctional protein substrates. Co-dependency analysis has the potential to identify functional relationships between genes by finding patterns in dependency across different cell lines with diverse underlying genetic contexts[32]. Exploring co-dependency relationships from CRISPR screen data in the Cancer Dependency Map (DepMap) datasets identifies a significant enrichment for KEGG and GO database tight-junction genes for PKN2 in bowel-lineage cells (Figure 5A-C) as well as the recently reported roles for PKN2 in the YAP (hippo) pathway [22,33]. Tight junction genes are not present in the top-co-dependencies for PKN1 or PKN3 suggesting this mechanism is specific to PKN2 (Figure S7A, B). Tight junction genes are also significantly overrepresented in the top co-dependencies for PKN2 in all adherent cells suggesting the mechanism of PKN2 in tight junctions is conserved across epithelial cells (Figure S7C-E). The polarity complex genes PARD3, PRKCI and PARD6B feature particularly at the top of the co-dependencies list for PKN2 (Figure 5A). PKN2 was previously identified as an interacting partner of PARD3 in Biogrid[34], in a PARD3 proximity ligation assay[35] and PARD3 was pulled down with the PKN kinase domain in rat brain peripheral membrane fractions [36]. The par complex proteins, particularly PARD3, have known roles in junction formation[37,38]. Network co-dependency analysis of the Par3-Par6-aPKC par complex across bowel-linage or all adherent cell lines identifies PKN2 as one of the central, highly connected key genes along with ZO-1 (TJP1) and TP53BP2 (ASPP2) (Figure 5D, S7F).

Overrepresentation analysis on previously published phospho-proteomics data indicates that perturbing PKN2 induces changes in the phosphorylation state to many junctional proteins (Figure S7G, H). To systematically assess the potential of PKN2 to phosphorylate junctional substrates we constructed an array of selected putative substrate peptides, and matched controls, from the top genes identified from co-dependency analysis; peptide sites included on the array were triaged for cellular occupancy (PhosphositeTM) and PKN kinase consensus-site scoring. The array was phosphorylated with recombinant PKN2-kinase domain and ATP [γ-^{32P}]. We also phosphorylated a parallel identical array with the established and closely related junctional kinase atypical PKCι [39] to explore specificity for PKN2 substrate recognition. Results identified that PKN2 can phosphorylate several sites in key high-codependency junctional proteins including Par3 and ASPP2 (Figure 5E).

We focused on the ASPP2 S737 site since it was not phosphorylated by PRKCI and represents a target of PKN2 in the ASPP2-PP1 complex with limited functional redundancy (Figure 5E). ASPP2 also shows the highest genetic co-dependency with PKN2, which indicates the highest potential for direct mechanistic interactions (Figure S7I). Previous studies demonstrated that ASPP2 recruits PP1 to regulate tight junction formation through the dephosphorylation of junctional targets including ZO1 and PAR3 [37,40-44]. The dephosphorylation of these targets is essential for unbinding of 14-3-3 proteins, liquid phase separation of ZO1 and formation of protein clusters in ZO1 and Par3 that seal tight junctions closed from initial cell contact sites [44-46]. Re-analysis of published ASPP2/PP1 pulldowns[43] identified PKN2, as well as it's activators RhoA and Rac1, but not PKN1 nor PKN3, complex with ASPP2 and PP1 (Figure S8A, B). PP1 catalytic subunits have also previously been pulled down with PKN kinase domain in rat brain cytosolic and peripheral membrane fractions [36].

AlphaFold aligns ASPP2 S737 with ATP in the kinase cleft of PKN2 but not PRKCI, consistent with ASPP2 being a substrate of PKN2 (Figure S8C). Multisequence alignment of 30 ortho and paralogues

of ASPP2 identify high evolutionary conservation of the S737 motif residing within an intrinsically disordered region of ASPP2 (Figure 5F, S8D, E) [47]. High conservation scores, in line with key PP1-interacting RVxF residues, imply the S737 site is a regulatory hotspot in the ASPP2-PP1 complex. One hypothesis, implied by protein multimer modelling, suggests the phosphorylated and disordered S737 ASPP2 region competitively blocks the PP1 active site, analogous to other PP1 regulators such as I-1, I-2, DARPP-32, CPI-17 and MYPT1 [48-51] (Figure 5F); this also predicts that the phosphorylated S737 site is a PP1 substrate. As both PKN2 and PP1 are recovered in complex with ASPP2, competition or sequential binding to the S737 site may contribute to the functional regulation of ASPP2-PP1 activity during tight junction assembly.

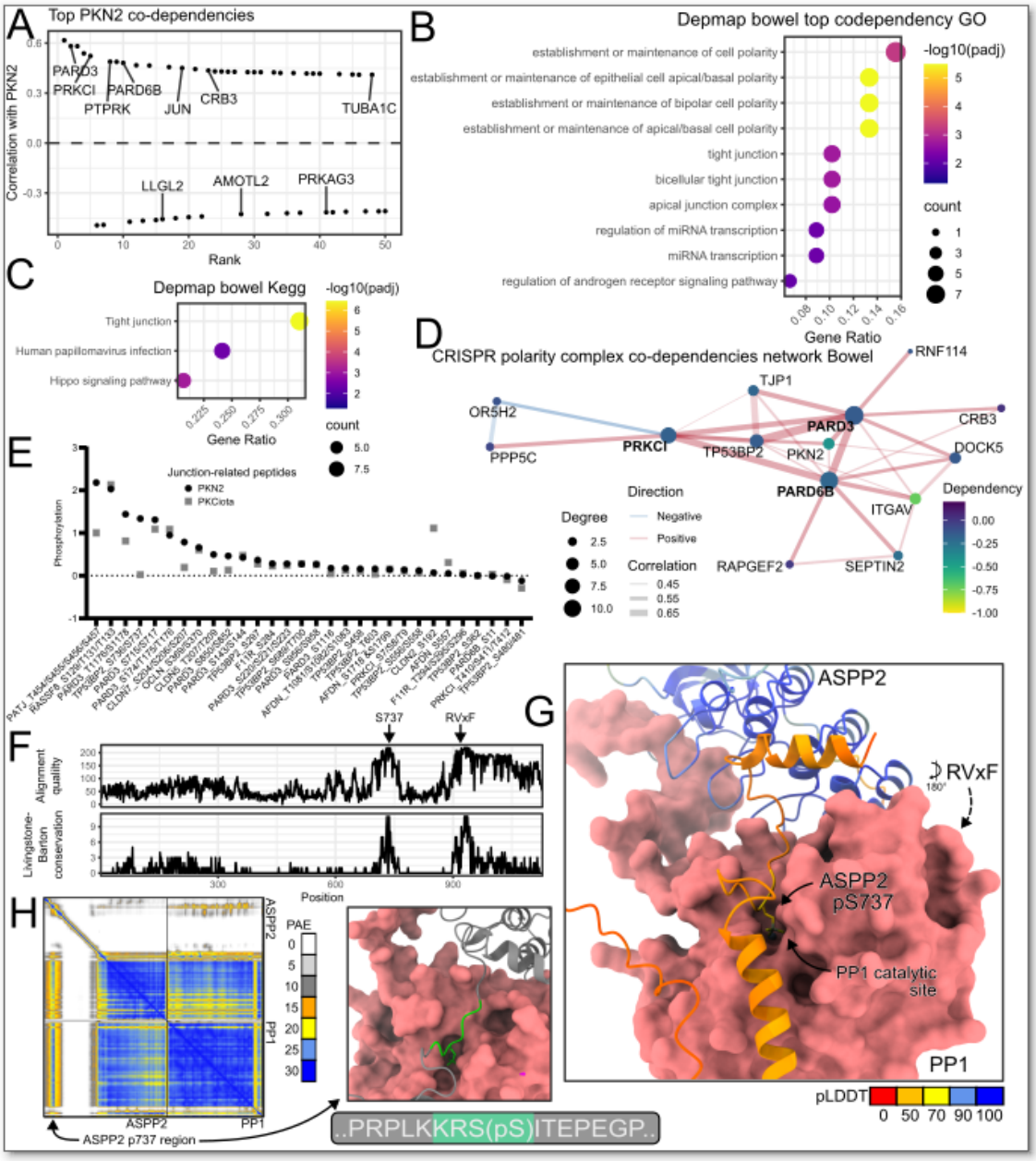

Figure 5: PKN2 regulates the ASPP2-PP1 complex in tight junction formation. A) The top co-dependencies for PKN2 in bowel-linage cells from CRISPR screen data from the Cancer Dependency

Map (DepMap) ranked by linear Pearson correlation coefficient. Genes in the GO:0034330 (cell junction organisation) and KEGG hsa04530 (tight junction) pathways are labelled. **B, C)** GO (B) and Kegg (C) term overrepresentation analysis on the top co-dependencies for PKN2 in all adherent cells as in A. **D)** Network analysis of the core Par complex genes PARD3, PARD6B and PRKCI highlighting their shared top co-dependencies in bowel lineage cells. Genes are represented as nodes and co-dependencies as edges. Nodes are sized by their degree and coloured by the genes mean individual dependency. Edge width corresponds with co-dependency strength between genes and coloured with direction. Network was assembled using the Fruchterman-Reingold layout algorithm. **E)** ATP [γ-^{32P}] and recombinant PKN2 kinase domain peptide phosphorylation array results with known junction related peptides identified as potential substrates of PKN2. Results are represented as z-scores. **F)** Multi-sequence alignment of 30 orthologues and paralogues of ASPP2 annotated with alignment quality and Livingstone-barton conservation scores. Conservation of S737 and RVxF regions are annotated with arrows. **G)** AlphaFold multimer modelling of the interaction between ASPP2 and PP1 (pink). ASPP2 is coloured with predicted local distance difference test (pLDDT) scores. The PP1 catalytic site and ASPP2 pS737 site are annotated. **H)** Predicted aligned error (PAE) plot from AlphaFold multimer modelling of the interaction between ASPP2 and PP1. High confidence region surrounding the pS737 site is highlighted (green).

Discussion

Our work identifies *PKN2* as a critical regulator of tight junction formation in the colon, protecting the bowel against inflammatory damage and CRC initiation. *PKN2*-targeted mice and primary organoids largely maintain morphologically intact tight junctions under homeostatic conditions, but significant defects emerge following epithelial injury, suggesting functional redundancy for normal tissue homeostasis. This concurs with knockout models of other core tight junction components, including O*CLN*, *JAM-A*, *PRKCI*, and *ZO-1*, which maintain homeostatic junctions at baseline but exhibit heightened sensitivity to inflammation and colitis [39,52-56]. These findings support the notion that homeostatic tight junctions are remarkably resilient to the loss of individual components, yet each contributes critically to maintaining barrier integrity during stress and epithelial repair.

Mechanistically, our research identified that PKN2 complexes with ASPP2 and PP1, a major phosphatase complex that dephosphorylates junctional targets including ZO1 and Par3. The dephosphorylation of ZO1 and PAR3 is reported to be essential for 14-3-3 unbinding, liquid phase separation and oligomerisation of junctional proteins [44-46]. In support of this we identified from previously published data that overexpression of active PKN2 kinase significantly increased the dephosphorylation of junctional targets. Our previous research also identified that PKN2 knockout in mouse embryonic fibroblasts results in increased phosphorylation of S174 and S221 in Par3 [21] suggesting a decrease in junctional phosphatase activity. We hypothesise that ASPP2 and PKN2 regulate PP1 activity in a similar way to other PP1 regulators such as CPI-17, which bind and block access into the active site of PP1. Several hypotheses for how intrinsically disordered PP1 inhibitor phosphoproteins regulate PP1 activity have been put forward including physical active site blocking, regulating subunit interactions, ion loading and unfair competition [48,49,57].

We propose that PKN2 phosphorylates ASPP2 S737 but may also phosphorylate other regulators of PP1 and cell junctions. CPI-17 T38, the major phospho-site that converts CPI-17 into an MLCP inhibitor, was previously identified as putative PKN2 substrate [58]. Further, the ASPP2 S737, alongside several Par3 sites were inhibited by the PKN2 and ROCK inhibitor Y27632[59,60]. Our experiments

provide additional evidence that PKN2 can potentially phosphorylate various junctional proteins including Par3, Claudins, Occludin and JAM-A.

Intriguingly, the H.pylori bacteriotoxin CagA, which is known to localise to and disrupt junction formation and cell polarity [61,62], directly binds to and inhibits the kinase activity of PKN2 and has also been resolved with an 80aa region of ASPP2 (726-782) containing the S737 site of interest [63,64]. Our research suggests that inhibition of PKN2 by CagA, in complex with ASPP2, may contribute to H.pylori pathogenesis and promotion of colorectal and gastric cancer.

PKN2 was also identified as one of 25 high-confidence candidate genes within CCs3, a locus associated with the heightened sensitivity of A/J mouse strain to AOM/DSS tumorigenesis, compared to C57BL/6J [65]. Further, PKN2 is among 340 genes within the *Cdcs1* locus, which contributes to enhanced susceptibility to disease in multiple genetic colitis models[20]. PKN2 has also been associated with increased risk of developing irritable bowel syndrome (IBS) in two genome-wide association studies (rs10923043, rs4656024) [63,64], and is one of 35 genes on a risk locus for human periodontitis (GS268364), a condition similarly linked to tight junction integrity and susceptibility to bacterial infiltration in the gums [65,66]. Here we show that loss of PKN2 alone is sufficient to confer sensitivity to both colitis and CA-CRC, establishing PKN2 as a key candidate gene on human chromosome 1p for susceptibility to IBD and CA-CRC. Strikingly, primary organoids from patients with IBD have a remarkable similarity in their expression profile to primary murine PKN2 knockout organoids, and PKN2 was identified as one of 18 significantly downregulated genes in endoscopic biopsies from patients with IBD when compared to healthy controls, alongside other junctional components such as PRKCI and CLDN8 [67]. This suggests deregulation to core junction components, including PKN2, is a key mechanism of human IBD pathogenesis. In addition, PKN2 lies within 207 genes on the Scc7 locus which confers susceptibility to DMH-induced sporadic colorectal cancer in the recombinant congenic strain CcS-3 compared with the more resistant BALB/c background [68]. This work highlights PKN2 as a candidate risk factor on human 1p in sporadic colorectal cancer, consistent with the poor prognosis observed in patients with 1p allelic loss.

Methods

Mouse models

Disease activity was quantified through a combined score of weight loss, stool consistency, haematochezia and general condition, scored 1-3 in each category with a maximum of 12 [24]. Mice with scores of 3 in either weight loss or general condition were subject to immediate sacrifice according to home office guidelines. Mice with scores of 3 in stool consistency or haematochezia were sacrificed if not recovered within 24h. Observations were performed semi-blind where genotypes were unavailable during periods of recording.

PKN2 knockout

Mice were treated with daily 100mg/kg intraperitoneal injections of tamoxifen (Sigma Aldrich) dissolved in corn oil (Sigma Aldrich) for five days and left for 20 days to allow for recovery and Cre-induced recombination of floxed sites around exon 8 of the PKN2 gene.

AOM/1%DSS model

The AOM/1%DSS model is outlined in Figure 1A. In brief, following 20 days recovery from tamoxifen treatment, mice received one intraperitoneal injection of 10mg/kg of azoxymethane (Sigma Aldrich) dissolved in PBS and filtered through a 0.45µm filter. Three days later the drinking water of mice was

treated with 1 or 2% dextran sodium sulphate (DSS) (MP Biomedicals) dissolved in distilled water. DSS is replenished after two days with freshly prepared DSS. Water bottle weight is taken to control for DSS uptake. DSS is replaced with fresh drinking water after five days of treatment and the mice are left to recover for 16 days. Identical second and third rounds of DSS treatment follow before allowing for tumours to develop for 40 days.

DSS only models

Following 23 days recovery from tamoxifen treatment the drinking water of mice was treated with 1 or 2% dextran sodium sulphate (DSS) (MP Biomedicals) dissolved in distilled water. DSS is replenished after two days with freshly prepared DSS. Water bottle weight is recorded to measure DSS uptake. DSS is replaced with fresh drinking water after five days of treatment and DSS effects are incubated for a further 3 or 10 days.

Immunohistochemistry and analysis

Colons were prepared according to the Swiss roll technique [69]. In brief, colons of mice were extracted between the cecum and rectum and were flushed with ice cold PBS using an oral gavage. Metal rods were inserted into the colon and a scalpel was used to slice along the length of the colon using the Swiss roll device. The colons were carefully flattened and sandwiched between filter paper. Samples were fixed in 4% formalin (CellPath) overnight and dehydrated in 70% ethanol for 2 days before being rolled into Swiss rolls, secured with needles and embedded in paraffin. Paraffin blocks were then cut into 5µm sections and fixed onto Superfrost slides.

Immunohistochemistry was performed by the Barts Cancer Institute pathology department and by study authors. Slides containing FFPE sections were dewaxed in xylene and hydrated using ethanol and water in a graded series. Antigen retrieval was conducted in boiling sodium citrate pH 6.0 10mM (VWR chemicals) for 10 minutes. Endogenous peroxidase was blocked using 3% hydrogen peroxide (Thermo Fisher Scientific) for 10 minutes, followed by protein blocking using horse serum and phosphate-buffered saline for 1 hour. Primary antibodies were incubated overnight at 4°C. The Universal Vectastain ABC kit was used for immunodetection. Secondary antibodies were selected based on the primary antibody and incubated for 1 hour at room temperature. 3,3′-diaminobenzidine tetra hydrochloride peroxidase (Dako, K3468) substrate was added until a brown colour was visible. Slides were counterstained using haematoxylin (Sigma Aldrich), then washed with tap water to remove excess dye. Slides were re-dehydrated by using graded increments of ethanol before being immersed in xylene. Coverslips were mounted onto slides using DPX (Sigma Aldrich).

The details of the primary antibodies used are as follows: CD4 (Thermo Fisher Scientific, 14-9766-82), CD8 (Thermo Fisher Scientific, 14-0808-82), F480 (Abcam, MCA497R), Ki67 (GeneTex, GTX16667), CD45 (Biolegend, 103101) and ZO-1 (Thermo Fisher Scientific, 617300). The details of other stains are as follow: Alcian Blue 8GX 1% in 3% Acetic Acid (RRSK400-100) for Alcian blue staining.

Slides were imaged using a Nanozoomer S210 (Hamamatsu) and analysis performed in QuPath (v0.5.1) [70]. The length of erosions, width of submucosa and number of regenerating crypts was averaged for each mouse across several histological sections at different depts. Areas of interest were selected using the wand and brush tools and positive cell detection used to test immune infiltrate. A random forest model was created in QuPath to quantify percentage area of positive alcian blue staining. Percentage area above a threshold of DAB staining intensity of a 18µm luminal strip was used to quantify ZO-1 junctional depletion.

PCR genotyping

To demonstrate PKN2 recombination in the crypts of *Pkn2*$^{fl/fl}$*;Vilin-CreER*^{T2} mice following tamoxifen treatment, colons were dissected, flushed with ice cold PBS, opened longitudinally and cut into 2mm segments. Tissue fragments were washed 15 times with ice-cold PBS and incubated with 2mM EDTA in PBS for 1h at 4°C. After removal of EDTA, tissue fragments were washed vigorously in cold PBS to release the crypts which were pelleted, and DNA extracted using the QIAamp mini-DNA kit (Qiagen) following manufacturer's instructions. Organoid samples were prepped by incubating organoid Matrigel domes in TrypLE (Gibco) for 10mins before pelleting the organoids and washing with PBS. DNA was extracted using the QIAamp mini-DNA kit (Qiagen) following manufacturer's instructions. DNA collection from embedded mouse bowels was carried out using GeneJET FFPE DNA Purification Kit on sections cut from an FFPE block (Thermo Fisher).

50ng DNA, Platinum™ II Hot-Start PCR Master Mix (Thermo Fisher) and 10µM of the following multiplex primers F: GCATGCTGAGGATGTCACCG, R1: GAGGGAAAATGGGAGAGG, R2: GCAGTGGTGAAGTCACATAC. PCR parameters were as follows: 94°C 3min, 94°C 20s, 60°C 30s x 35 cycles, 72°C 45s, 72°C 5 min and 4°C hold. Samples were run alongside a 50bp ladder (NEB), on a 6% TBE gel (Thermo Fisher) at 90v for 90mins. Gels were incubated in GelGreen (Merck) for 15mins before being imaged on a ChemiDoc MP (Bio-Rad).

Cell Lines

Caco-2 were a gift from the Egle Solito lab. HEK 293T and DLD1 were sourced from American Type Culture Collection (ATCC). L-WRN cells developed by Takahashi et.al. were a gift from the Chris Tape Lab.

Cell culture

DLD1 and L-WRN were cultured in Dulbecco's modified Eagle's medium (DMEM) (Gibco) containing 10% fetal bovine serum (FBS) (Gibco) and 100 U/ml penicillin/streptomycin (Gibco), which was changed every 2 days. Caco-2 cells were cultured in DMEM (Gibco) containing 10% FBS (Gibco), Non-essential Amino Acids (NEAA) (Gibco), 10% Glutamine (Gibco) and 100 U/ml penicillin/streptomycin (Gibco). HEK 293T cells were cultured in DMEM+Glu (Gibco) containing 10% FBS (Gibco). Cell lines were cultured at 37oC with 5% CO2 in T75 or T175 flasks (Gibco). Cell lines were sub-cultured by dissociation with 0.1% (w/v) Trypsin-EDTA (Gibco) at 37°C for 3-5 minutes. Cells were stored long term in liquid nitrogen in storage medium consisting of 90% (v/v) FBS and 10% (v/v) DMSO (Sigma) or Gibco™ Recovery™ Cell Culture Freezing Medium (Gibco).

Organoid production and culture

Colonic organoids were generated as described in Qin, 2020[71]. Briefly, the colons of 12-week-old wild-type C57BL/6 and *Pkn2*$^{fl/fl}$*;Rosa26-CreER*^{T2} mice were dissected, flushed with ice cold PBS, opened longitudinally and cut into 2mm segments. Tissue fragments were washed 15 times with ice-cold PBS and incubated with 2mM EDTA in PBS for 1h at 4°C. After removal of EDTA, tissue fragments were washed vigorously in cold PBS to release the crypts. Supernatant fractions were collected and centrifuged at 290xg for 5min. Cells were washed with 15ml of advanced DMEM/F-12 (Gibco), passed through a 100-µm cell strainer to enrich for intestinal crypts and centrifuged at 290xg for 2min. The cell pellet was resuspended in 100% Growth Factor Reduced Matrigel (Corning) at a density of 200 crypts per 40µl Matrigel and cultured at 37°C in the presence of 5% CO_2.

The base culture media consisted of: Advanced DMEM/F-12, (Gibco), 2mM L-glutamine (Gibco), 1mM N-acetyl-l-cysteine (Sigma), 10mM HEPES (Sigma), 1X B-27 supplement (Gibco, 50X), 1X N-2 supplement (Gibco, 100X) and 1× HyClone Penicillin Streptomycin Solution (Cytiva). The base media was further supplemented with 10mM nicotinamide (Merck), 50ng mL−1 mEGF (PeproTech) and 25%

WRN-conditioned media, which replaces 100ng⍰ml−1 murine WNT-3a, 50ng⍰ml−1 mNoggin and 500ng⍰ml−1 mR-Spondin-1.

To passage the colonic organoids, organoids were dissociated mechanically by pipetting. Organoid fragments were collected using a benchtop centrifuge, washed with ice-cold PBS 3 times and reseeded in fresh Matrigel. The passage was performed every 7-10d at a ratio of 1:1.5-1:2. Inducible PKN2 KO was initiated in the organoids by addition of 2µM 4-hydroxytamoxifen (TAM) (Merck) for 7 days.

WRN Conditioned media
L-WRN cells developed by Takahashi et.al. were a kind gift from the Chris Tape Lab, with permission from the Shinta Sato lab[72]. L-WRN cells were expanded to confluency in a T175 flask in DMEM (Gibco) containing 10% fetal bovine serum (Gibco) and 100U/ml Pen-Strep (Gibco). Harvested as described previously and plated into a Hyperflask (Sigma) with 500ml media and allowed to expand to 70-80% confluency. Media was replaced and incubated for 72h before harvest and filtered using a Stericup system (Millipore). The conditioned media was then aliquoted and stored at -80°C.

CRISPR

Generation of custom gRNA expression vectors

Human PKN2 gRNA was designed using ChopChop, Guide H2 – CTTTGACGTGGACTTAGTGT (Exon 6). The control gRNA sequence used (GTATTACTGATATTGGTGGG) was described in Doench et.al[73]. The control and H2 guides were ligated into the Lenti-Cas9-gRNA-GFP plasmid (Addgene #124770), a gift from Jason Sheltzer (Addgene plasmid #124770) as described in Giuliano et.al[74]. In brief, the Lenti-Cas9-gRNA-GFP plasmid was linearised with BsmBI-v2 enzyme (NEB) and purified from an agarose gel using the QIAquick gel extraction kit (Qiagen). The forward and reverse primer sets for each guide (H2F – caccgCTTTGACGTGGACTTAGTGT, H2R – aaacACACTAAGTCCACGTCAAAGc, CtrlF – caccgGTATTACTGATATTGGTGGG, CtrlR - aacCCCACCAATATCAGTAATACc) were annealed together by gradual cooling from 95°C to 30°C using T4 PNK (NEB). The annealed primers were ligated to the linear plasmid using T4 ligase (NEB) at room temp for 30 minutes. The ligated plasmids were incubated with 25µl Stbl3™ Cells (Thermo Fisher) for 45mins on ice, heat shocked at 42°C for 45 sec and added to 400µl SOC media (Thermo Fisher), shaken at 37°C for 45mins, and plated out onto LB-Amp plates (100µg/mL ampicillin). Three colonies were cultured, plasmid extracted using a QIAprep miniprep kit (Qiagen) and sent for Sanger sequencing (U6 primer). Correct clones were grown in 100ml overnight LB culture and extracted using the NucleoBond Xtra Midi prep kit (Macherey-Nagel) ready for lentivirus production.

Lentivirus Production and infection

HEK293T cells were cultured as described previously, harvested, and $4x10^6$ cells were plated per T75 flask and allowed to attach overnight. Media was changed (8ml) the following morning, and after 5 hours, a lentivirus transfection was prepared for each gRNA plasmid. In the following order, H_2O (up to 625µl), 4.5µg pMD2.G (Addgene #12259), 3.2µg pRSV-Rev (Addgene #12253), 6.3µg pMDLg/pRRE (Addgene #12251), 7.5µg pAdVAntage (Promega), 15µg gRNA plasmid and 78.1µl 2M CaCl2 (ProFection) were added to a 14ml falcon and vortexed. 625µl of HeBS pH 7.1 was bubbled through the solution for 30 seconds using an automatic pipettor. After 10 minutes the solution was added to the T75 flask of HEK cells. Media was changed after 12-16 hours. After 24 hours, the virus containing media was harvested, filtered (0.45µm) and either added to cells immediately at a 1:1 ratio with media or frozen at -80°C.

DLD1 cells were harvested, and 600,000 cells/well were added to 6 well plates. 2ml of media was added to a control well. 1ml of PKN2 H2 and control gRNA virus were added at a 1:1 ratio with normal cell media and 8µg/mL Polybrene. 24 hours later, the virus media was removed and replaced with normal cell media. Cells were expanded into T75 flasks before being harvested for GFP+ cell sorting.

Cell Sorting

Cells were harvested as described previously and centrifuged at 300g for 3 minutes. Cells were resuspended in FACS buffer (1xPBS, 3mM EDTA, 25mM HEPES pH 7.0 and 1%FBS), strained through a 50µm filter and moved to ice. 0.1mg/ml DAPI was added at 1:1000 dilution just before sorting for live cell gating. GFP+ cells were sorted on an ARIA Fusion and collected in 1:1 ratio FBS:Media, centrifuged as before and added to an appropriate size plate/flask. After recovery and expansion, the H2 polyclonal PKN2 KO line was further dilution plated, and single clones were collected for confirmation of PKN2 KO.

Inducible DLD1 cells

Stable inducible DLD1 (iDLD1) cells were produced using the Flp-In™ T-REx™ system (Invitrogen). Wild type PKN2 (Wt-PKN2) and kinase dead PKN2 (D782A) (KD-PKN2) constructs were inserted in DLD1-FRT cells (Gifted by Prof Stephen Taylor) that have a stably expressed Tet repressor and a single integrated FRT site. The pcDNA5/FRT/TO/PKN2-Construct expression vectors (50ng/ml) were co-transfected with 450ng/ml pOG44 (Thermo Fisher Scientific) using 0.25µl/ml PLUS™ reagent (Thermo Fisher Scientific) and 1µl/ml Lipofectamine™ LTX (Thermo Fisher Scientific) diluted in Opti-Minimal Essential Medium (Opti-MEM, Gibco) according to manufacturer's instructions into 70% confluent DLD1-FRT cells plated onto 10cm dishes (Corning). Following a two-day incubation, cells were serially cultured in 100µg/ml hygromycin (Invitrogen) and 10µg/ml blasticidin (Thermo Fisher Scientific) supplemented culture medium for 30 days to allow for selection. iDLD1 cells were induced with 500ng/ml tetracycline (Sigma) dissolved in 100% ethanol and diluted in regular culture media.

siRNA treatment

100,000 DLD1 cells were seeded in 24-well plates with round glass coverslip inserts. After 24h to allow for adhesion, they were then incubated with 20nM siRNA control (siCtrl #1 and siCtrl #Luc) or PKN2 (siPKN2 #9, 10 & 11) pools (GE HealthCare), 0.25µl/ml Plus reagent, 2µl/ml Lipofectamine LTX (Invitrogen) per well, diluted in Opti-Minimal Essential Medium (Gibco) for 3 days before being fixed with PFA and stained for PKN2 and ZO-1 as described previously.

Transwell assays

12mm Transwells with 0.4µm Pore (Corning) in 24 well receiver plates were hydrated with DMEM, no Phenol Red (Gibco) containing 10% fetal bovine serum (Gibco) and 100U/ml Pen-Strep (Gibco) in the transwell and receiver plate for 15mins. 15k DLD1 cells were then seeded and left to expand for 7 days under normal culture conditions. 50mg/ml DSS for 2h, 4mM EGTA for 30mins or normal media control were added to their respective Transwells and receiver plates. After incubation, the media in the transwell and receiver plate was changed to wash away treatments. The transwells were moved to a new receiver plate with 600µl media in the bottom compartment and transwell media replaced with 40kda FITC Dextran at 5mg/ml (Merck) in media. After 3h, 2x 50µl samples from the receiver plate were taken and fluorescent intensities measured on a FLUOstar OPTIMA microplate reader (BMG LABTECH) at 485nm and 535nm excitation and emission.

Immunofluorescence

10-15k DLD1 cells per well were seeded onto sterile 14mm coverslips in a 24-well plate (corning) or directly onto 96-well PhenoPlates (Revvity) and left to establish for 4 days. Cells were then either transfected with siRNA, DNA or induced with tetracycline.

Cell monolayers were washed with PBS and fixed in 4% PFA (Pierce 16% Formaldehyde, Thermo Fisher) in PBS for 15 mins then permeabilised in 0.2% Triton X 100 (Sigma) in PBS for 15 mins. Fixed monolayers were blocked in 5% BSA (Sigma) for 1h and then incubated with primary antibodies overnight at 4°C. As PKN2 antibody staining is weak, amplification was achieved using Alexa Fluor™ 488 or 555 Tyramide SuperBoost (Invitrogen) according to the manufacturer's instructions. Following washes with PBS, samples were incubated for 1h in secondary antibodies and DAPI. Coverslips were mounted onto slides using MOWIOL 4-88 mounting medium and 96 well plates in PBS. Fluorescence was visualised using LSM 710/880 confocal microscope (Zeiss) or high content microscope IN Cell Analyzer 6000 (Cytiva) and images were analysed using Fiji ImageJ (v2) or CellProfiler (v4.2.8) [75].

Organoids were plated in 3D 40ul droplets on Nunc Lab-Tek II 8 well Chamber Slides (Thermo Fisher) and grown for 4-5 days. Washed with PBS, Fixed 4% PFA (Pierce 16% Formaldehyde, Thermo Fisher) for 2h, permeabilised with 0.5% Triton X 100 (Sigma) for 15 mins. Washed with PBS, blocked with 4% BSA (Sigma) for 1h. Incubated with primary antibodies overnight at 4°C. Tyramide was added as described previously for 15 mins. Following washes with PBS, samples were incubated for 1h in secondary antibodies and DAPI. After removal of the slide chamber, coverslips were mounted onto slides using MOWIOL 4-88 mounting medium. Fluorescence was visualised using LSM 880 confocal microscope (Zeiss).

Primary antibodies: PKN2 (R&D, MAB5686), ZO-1 (Invitrogen, 61-7300), E-cadherin (Cell Signaling Technology, 3195T), Phalloidin (Invitrogen, A22283). Secondary antibodies: Donkey anti-Rabbit IgG Alexa Fluor™ 488 (Invitrogen, A-21206), Donkey anti-Rabbit IgG Alexa Fluor™ 555 (Invitrogen, A-31572), Goat anti-Rabbit Alexa Fluor™ 633 (Thermo-Fisher Scientific, A-21071), Goat anti-Mouse IgG Alexa Fluor™ 488 (Invitrogen, A-11001) or Donkey anti-Mouse IgG Alexa Fluor™ 555 (Thermo-Fisher Scientific A-31570).

Junctional staining analysis

A custom built CellProfiler (v4.2.8) [75] pipeline was assembled to perform junctional analysis. In brief, ZO1 stained junctions were processed using morph "openlines" with a line length of 30 and "neurite like" features were enhanced with the "tubeness" method and a smoothing scale of 2. Processed junctions were smoothened with a circular average filter and diameter of 4 before a threshold was applied using the global robust background method. The Boolean image was converted into CellProfiler objects and junctions were filtered ensuring a minimum major axis length of 5.4µm to remove punctate artifacts. Measurements were taken from filtered junction objects and the original ZO1 image was masked with junction objects to measure junctional ZO1 intensity.

Molecular biology

Western blotting

Fresh tissue was collected and snap frozen on dry ice. Frozen tissue was broken up into a powder with a pestle and mortar cooled on dry ice. The powder was lysed with 1xLDS and 50mM DTT (Sigma-Aldrich), sonicated for 30 seconds and boiled at 95°C for 5mins. 15µl of sample was loaded into a NuPAGE 4-12% Bis-Tris gel (Invitrogen) in tris-glycine SDS and run at 120v for 2h. Gels were wet transferred onto nitrocellulose membrane (Amersham) in tris-glycine 20% methanol overnight at 30v.

Cells were washed with PBS and lysed in sample buffer (3% (w/v) SDS, 60mM sucrose and 65mM Tris, PH 6.8), sonicated for 30 seconds and centrifuged at 4°C for 10 mins at 16,000g. Protein concentrations were measured against known controls on a colorimetric microplate reader (Tecan) at 750nm using a Bio Rad DC protein assay kit, according to the manufacturer's instructions. Samples were diluted in 4X NuPAGE LDS (Invitrogen), 100mM dithiothreitol (DTT) (Sigma-Aldrich) and sample buffer and boiled at 95°C for 3 minutes. 20-30µg of protein was separated by NuPAGE 4-12% Bis-Tris gel electrophoresis in NuPAGE MOPS buffer (Invitrogen) for 1h at 120V and 30m at 150V, alongside 6µl Precision Plus Protein Dual Color Standards (Bio Rad). Blotting onto PVDF membrane (Millipore) was run at 28V overnight or 90 minutes at 100V at 4°C.

For both, membranes were washed TBS-tween (0.1%) (Severn Biotech) and blocked in 3% BSA (Sigma) in TBS-tween (0.1%) for 2h before being incubated with anti-PKN2 antibody (R&D MAB5686 or Sigma MABT496), GAPDH (Santa Cruz SC-25778) or HSC70 (Santa Cruz SC-7298) antibody diluted in blocking buffer overnight on a rocker at 4°C. The following day, membranes were washed with TBS-tween (0.1%) and incubated with anti-mouse HRP secondary antibody (GE Healthcare NXA931) for 2h at room temperature. Blots were washed again with TBS-tween (0.1%) and developed using chemi-luminesence methods, Luminata Forte (Merck) for PKN2 and Luminata Crescendo (Merck) for GAPDH and HSC70. Images were taken using an Amersham Imager 600.

Membrane PKN2 substrate array

Junctional genes of interest were manually selected due to their presence in co-dependency analysis and/or relevant literature. Potential substrate sites for PKN2 were identified from PhosphoSitePlus[76]. Amino acids flanking the serine/threonine of interested were identified from UniProtKB (v2023_03) [77] in the following configuration n-6aa-s/t-5aa-c-. Phosphorylation sites at the beginning or end of the peptide were shifted so that their sequence window fills the 12aa peptide length.

A positive control synthetic substrate for PKN2, NS1[78], was used as a positive control. Each peptide was also controlled for non-substrate-specific ATP binding with a peptide that had any serine/threonine +/-3aa flanking the serine/threonine of interest substituted to an alanine. Two peptide arrays were printed onto a cellulose sheet at the chemical biology science technology platform at the Francis Crick Institute. Membranes were blocked overnight in 0.2mg/ml BSA (Sigma) 20mM Tris pH 7.5, and 0.02% Tween-20 at 4°C. Each membrane was incubated with recombinant 10ug PKN2 (MRC PPU reagents and services, DU1658) or PKCι (courtesy of Niel McDonald laboratory) kinase domain in 20mM Tris, pH 7.5, 10mM MgCl2, 0.01% Triton X-100, 50µM EGTA, pH 8 and 1mM DTT. To start reaction, 150µl 10mM ATP spiked with 7.5µl ATP[γ-^{32P}] (Revvity, BLU502A250UC) and incubated on rocker for 10mins. The membranes were washed with 30% acetic acid for 1h before being imaged on the Packard (PerkinElmer) cyclone phosphor imager. Membranes were then washed with 0.1M NaOH for 1h before being imaged again.

Membrane spots were quantified using the protein array analyser (v1.1.c) for ImageJ. To estimate relative levels of kinase phosphorylation the alanine control peptides were subtracted from their non-control peptides and scaled into z-scores by dividing the samples by the standard deviation of the dataset. Membrane spots from different wash conditions with the greatest difference between the S/T and alanine control were used.

RNA sequencing and bioinformatic analysis

All RNA sequencing FASTQ files for mouse adenomas, cell lines and organoids are deposited onto the Gene Expression Omnibus (GEO) under project accessions GSE313373, GSE313374, GSE313375 respectively.

All RNA sequencing and bioinformatic analysis was performed using custom R (V4.4) or bash scripts available on GitHub (https://github.com/jackchenry/PKN2_in_CA-CRC).

Standard RNA sequencing

Cells and organoids were washed with PBS, lysed and RNA extracted using the Qiagen RNAeasy mini kit (QIAGEN) as per manufacturer's instructions. RNA quality and integrity was assessed using a Qubit (Thermo Fisher Scientific) and 5300 Fragment Analyzer (Agilent Technologies) with a DNF-472T33 - HS Total RNA kit (Agilent Technologies). Poly(A) selection Library preparation and paired-end RNA sequencing was performed by GENEWIZ (Azenta) using the NovaSeq™ 6000 platform (Illumina).

The quality of fastq files were assessed using fastqc (v0.11.9) and multiqc (v1.25.1). Sequencing adapters were trimmed from reads using trimmomatic (v0.36). Reads were aligned to GRCm39 for organoid samples and GRCh38 for human DLD1 samples using STAR (v2.7.9a). BAM files were sorted and indexed using samtools (v1.19.2) and counted using featureCounts from subread (v2.0.6) in unstranded mode on gene regions using annotation files from ensembl (GRCh38 112) and GENCODE (M34).

Smart3seq RNA sequencing

Laser capture microdissection (LCM) was carried out on 10µm FFPE sections cut onto UV-treated polyethylene naphthalate (PEN) membrane glass slides (Thermo Fisher ARCTURUS™, LCM0522). Slides were dewaxed using xylene and stained with methylgreen to identify epithelium. Approximately 150,000μm^2 sections of epithelial tissue were laser captured using a Leica LMD7 microdissection microscope. The area for laser capture was cross-referenced with the corresponding H&E section that was annotated by our collaborating pathologist (Marnix Jansen). Images at x2.5 and x10 were taken of each slide before and after laser capture to demonstrate that the appropriate section was sampled.

Smart-3SEQ library preparation was conducted in accordance with the "fresh frozen" version of the Smart-3SEQ protocol[25]. Some modifications were made to the published protocol as follows: 7 nucleotide unique molecular identifiers (UMIs) were used, and the lysis time was increased to 60 minutes at 70°C as per prior optimisation in the McDonald laboratory[79]. The 1S primer was used at a 20µM concentration. The PCR was run for 18 cycles. This required prior rounds of optimisation (from 15 to 18 cycles) to assess DNA quantity and quality. Once the assay was optimised, 3 batches of LCM samples were run. The quality and quantity of the pooled DNA library was assessed using a Tapestation Fragment Analyser (Agilent Technologies) with the HSD1000 ladder (5067-5587), HSD1000 reagents (5067-5585) and HSD1000 sample buffer (5067-5603). The pooled library was sent to the Genome Facility at the Institute of Cancer Research (ICR) for single-end sequencing using the Illumina NextSeq 2000 platform (P2 kit for 100 cycles). The pooled library was also demultiplexed by the Genome Facility (ICR).

The quality of fastq files was assessed using fastqc (v0.11.9) and multiqc (v1.25.1). Sequencing adapters and low-quality reads were trimmed using trimmomatic (v0.36). Reads were aligned to GRCm39 using STAR (v2.7.9a). BAM files were sorted and indexed using samtools (v1.19.2) and deduplicated using umi_tools (v2.0.6) in python (v3.6.3). Reads were mapped to genes using featureCounts in strand specific mode using annotation files from GENCODE (M34) before being counted using umi_tools.

RNA sequencing analysis

Differential gene expression analysis was performed using the R package DeSeq2 (v1.44)[80]. Gene set enrichment analysis was performed using the R package fgsea (v1.30)[81] on ranked test statistics using gene sets obtained from the molecular signatures database (v2024.1.Hs; 2024.1.Mm)[82]. Graphs were plotted with ggplot2 (v3.5.1)[83] and heatmaps with ComplexHeatmap (v2.20)[84]. All

TCGA RNA sequencing data was obtained from the Genomic Data Commons data portal (https://portal.gdc.cancer.gov/). Human colitis patient organoid RNA sequencing data was obtained from the Gene Expression Omnibus (GEO accession: GSE102746)[31]. Known and candidate cancer genes were obtained from the Cancer Gene Consensus (CGC, COSMIC)[36].

Single cell

All single cell RNA sequencing data was obtained from the Single Cell Portal from the Broad Institute. Single cell RNA sequencing data from treatment-naive paediatric Crohn's disease and uninflamed control patients with a functional gastrointestinal disorder was obtained from the PREDICT 2021 cohort (Single Cell Portal accession: SCP1423, SCP1422)[85]. Diseased colon epithelial, stromal and immune cell data was obtained from the Human Crohn's disease atlas (Single Cell Portal accession: SCP1884)[86] and the Ulcerative colitis atlas (Single Cell Portal accession: SCP259)[87]. Diseased colorectal cancer cell data was obtained from the Human Colon Cancer Atlas (Single Cell Portal accession: SCP1162)[88]. All single cell data used t-SNE and UMAP coordinates calculated in their respective studies but have uninflamed control cells removed where applicable.

ARCHS4 prediction analysis

PrismEXP prediction results on ARCHS4 data was obtained for PKN2 from the ARCHS4 data portal (v2.5, https://archs4.org/)[89] for the Human Phenotype Ontology, MGI Mammalian Phenotype (Level 4 2021) and KEGG (2021 Human) collection of gene sets from Enrichr.

The cancer dependency map CRISPR screen analysis

CRISPR screen data was obtained from the 24Q4 release of DepMap from the DepMap data portal from the Broad Institute (https://depmap.org/)[66]. Co-dependency analysis was conducted by performing pairwise complete Pearson correlation between PKN2 and genes of interest. Overrepresentation analysis was performed using enrichGO and enrichKEGG from clusterProfiler (v4.10.1) Networks were plotted with iGraph (v2.0.3) using genes as nodes and codependencies as edges. Gene pair codependencies less than 0.44 were not plotted for bowel linage cells and less than 0.26 for adherent lines. Networks were arranged using the Fruchterman-Reingold algorithm.

PKN2 mass spectrometry analysis

The PKN2 mass spectrometry analysis comparing overexpression of a deregulated truncated PKN2 with a kinase dead PKN2 in HEK293 cells was obtained from the source publication[33]. Overrepresentation analysis was performed using enrichGO and enrichKEGG from clusterProfiler.

ASPP2 and PP1 pulldown affinity purification mass spectrometry analysis

Affinity purification-mass spectrometry data using baits for ASPP2 and PP1 in HEK293 cells was obtained from ProteomeXchange database (ID: PXD012378)[43]. The relevant abundance of each protein was normalised to the bait protein of that sample and scaled to uncentred z-scores across the samples. Heatmaps were plotted in R with ComplexHeatmap (v2.20)[84].

Multi-sequence alignment

ASPP2 orthologues and paralogues were selected using the ensembl comparative genomics database. UniProt sequences were identified for the Ensembl Canonical entry. Multi-sequence alignment was performed using Clustal Omega from EMBL-EBI job dispatcher. Alignments were analysed using R and Jalview (v2.11.5.0). The Blosum62 alignment quality and Livingstone-barton conservation scores were calculated in Jalview. IUPred intrinsically disordered region scores were calculated using the IUPred web service client. Valdar and Shenkin conservation scores were calculated using AACon web service client.

AlphaFold analysis

Protein folding modelling was performed using AlphaFold-Multimer using the AlphaFold Server web services client. Protein sequences were obtained from UniProt. Post-translational modifications to PKN2 kinase include pT816 and pT958 and to PRKCι include pT412 and pT564 of their activation loops and turn motifs respectively. Images of protein structures were arranged using ChimeraX (V1.9).

Acknowledgements

We thank the core services at the Barts Cancer Institute, including Biological Services, Animal Technician Services, Pathology, Preclinical Imaging, and Microscopy. We are also grateful to Queen Mary's Apocrita HPC facility, supported by QMUL Research-IT, and to the Phenotypic Screening Facility at the Blizzard Institute. We acknowledge the Genomics Facility at the Institute of Cancer Research and the Chemical Biology Science Technology Platform at the Francis Crick Institute for their support. We extend our thanks to Professor Jane Sosabowski for assistance with radioactive assays, and to Nic Tapon and Teresa Bertran for providing constructs and valuable advice. We also thank Professor Peter Parker for his help in developing the PKN2-targeted mice. Finally, we are grateful to the laboratories of Chris Tape, Shinta Sato, and Egle Solito for supplying L-WRN and Caco2 cells.

Author contributions

J.C.H. and A.J.M.C. conceptualised and developed the study. J.C.H performed the majority of experiments and analysis. A.C. contributed cell based and organoid studies. J.C.H. and P.H. conducted RNA sequencing, tissue staining and analysis with help from A.P., K.S. and M.L. J.C.H, J.S., S.M. and A.J.M.C. contributed to in vivo experiments. I.R. and A.J.M.C. conducted mouse model development. M.J. and S.M. assisted with pathology and analysis. N.Q.M supported peptide array development and analysis. T.G. And S.M. supported project development and data collection. J.C.H. and A.J.M.C wrote the manuscript with comments and approval from all the authors.

Competing interests

The authors declare no competing interests.

Materials and correspondence

Angus JM Cameron. e-mail: a.cameron@qmul.ac.uk

Supplemental

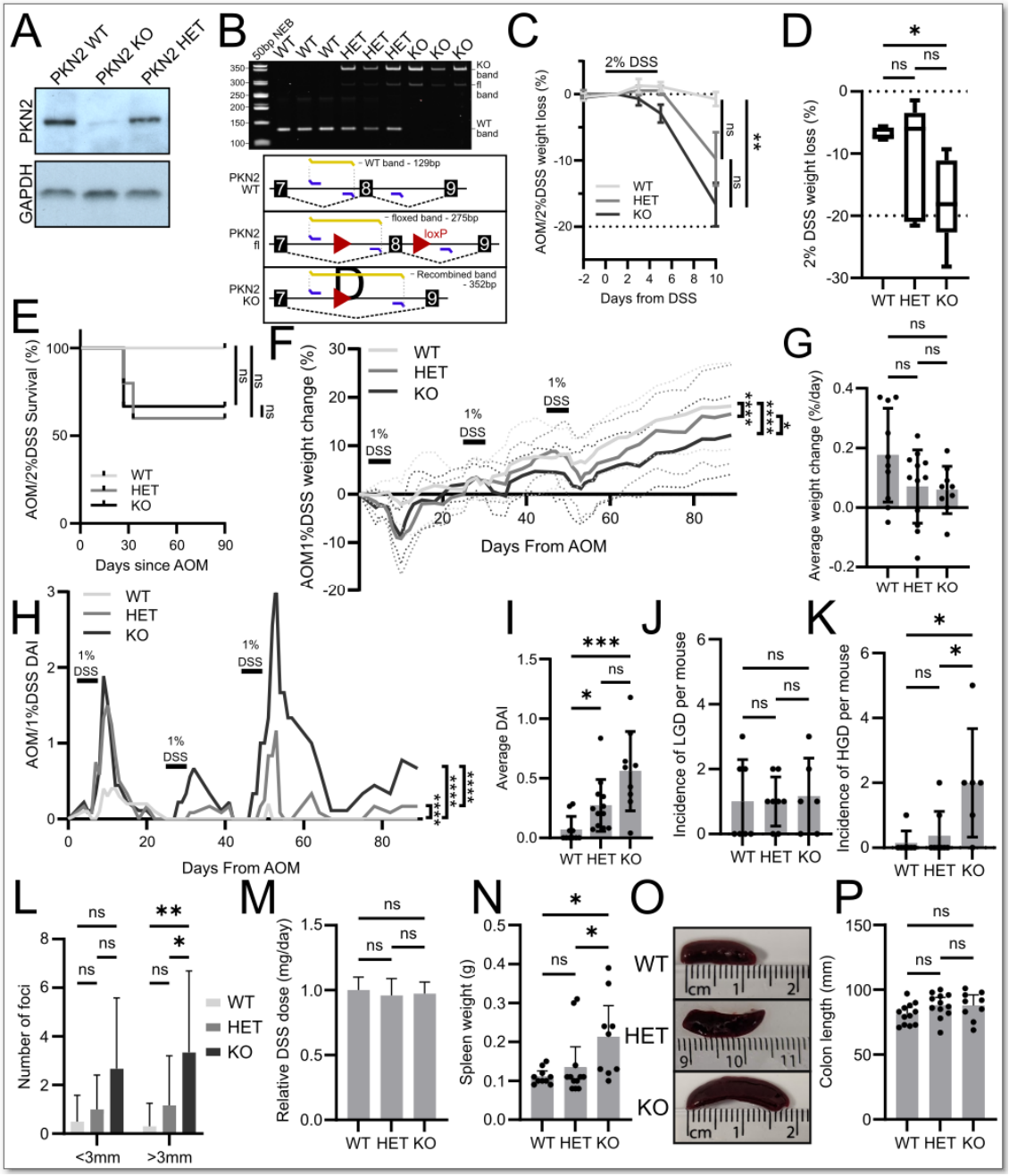

Figure S1: PKN2 loss sensitises mice to DSS treatment. A) PKN2 protein expression of intestinal tissue determined by western blot following the tamoxifen treatment regime. **B)** PCR genotyping of intestinal tissue two weeks following the tamoxifen treatment regime of global-iPKN2^{KO} mice. Schematic describing the primer strategy and expected band sizes is shown in the bottom panel. **C, D)** Average (C) and maximum (D) weight loss in response to the first 10 days of AOM/2%DSS treatment in WT, HET and PKN2 KO mice (WT: n=5, HET: n=5, KO: n=6). Statistical significance was determined using a two-way repeated measures ANOVA (C) or a Dunn's multiple comparisons test (D). E**)** Survival of WT, HET and PKN2 KO mice in response to 1 dose of 10mg/kg AOM followed by 5 days treatment with 100mg/kg tamoxifen and 1 round of 2%DSS for five days (WT: n=17, HET: n=18,

KO: n=17). Statistical significance was determined using a Log-rank test. **F-I)** Average weight loss (F, G) and disease activity scores (H, I) across the second and third rounds of 1%DSS treatment in WT, HET and PKN2 KO mice (WT: n=10, HET: n=12, KO: n=9). Statistical significance was determined using a two-way repeated measures ANOVA (F, H) or a Dunn's multiple comparisons test (G, I). **J, K)** Quantification of low (LGD, J) and high-grade dysplasia (HGD, K) in WT, HET and KO adenomas formed from the AOM/1%DSS treatment protocol (WT: n=7, HET: n=8, KO: n=6). **L)** The average number of small (<3mm) and large (>3mm) diameter macroscopically visible adenomas from the AOM/1%DSS protocol across WT, HET and PKN2 KO mice (WT: n=10, HET: n=12, KO: n=9). **M)** Relative average DSS dose measured through water bottle weight across WT, HET and PKN2 KO mice (WT: n=10, HET: n=12, KO: n=9). **N-P)** Representative image of spleen size (O) and average weight (N) and average colon length (P) in WT, HET and PKN2 KO mice following the full the AOM/1%DSS protocol (WT: n=10, HET: n=12, KO: n=9). Statistical significance was determined using a Tukey's multiple comparisons test.

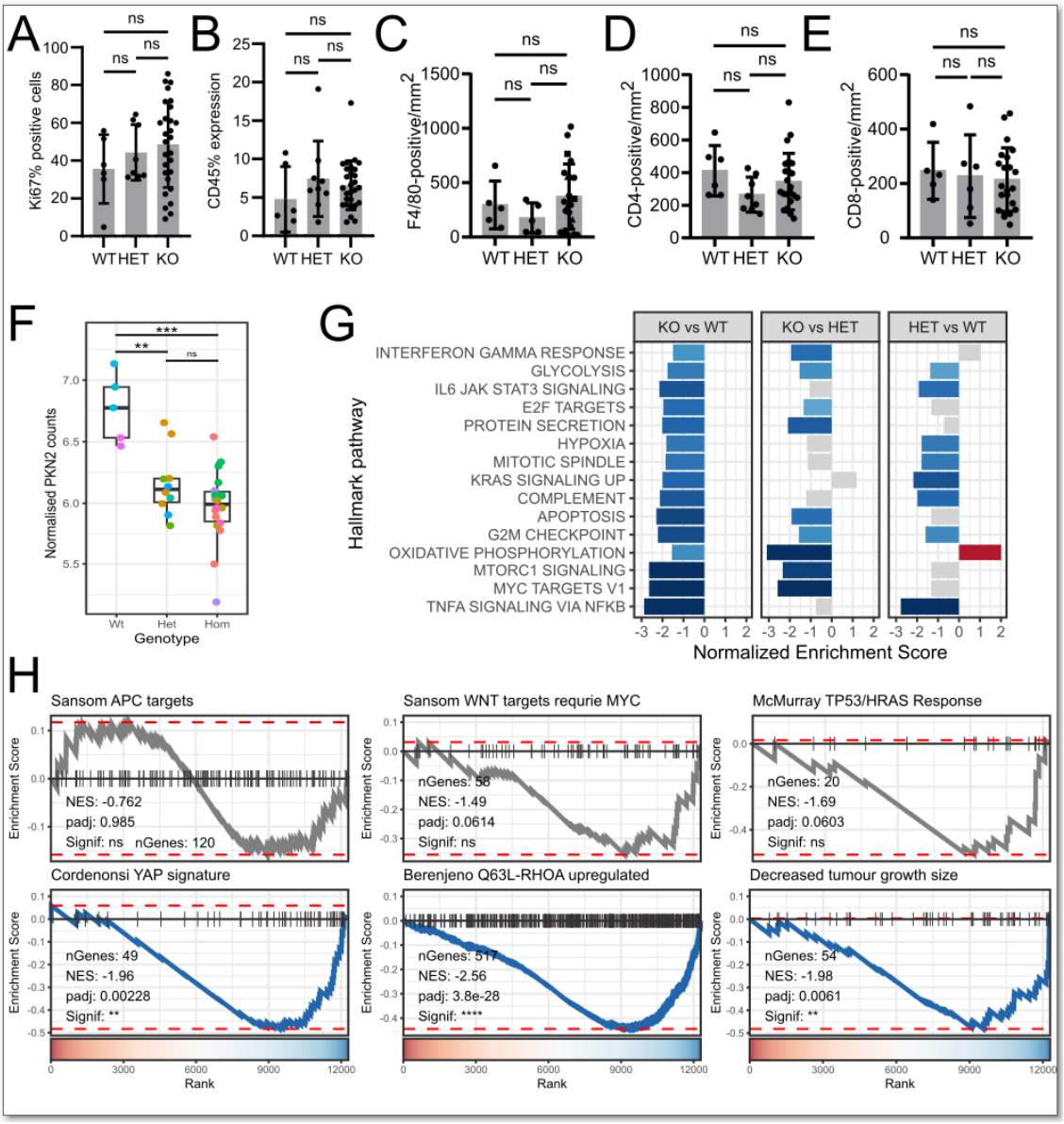

Figure S2: PKN2 status does not dictate tumour phenotype. A-E) Immunohistochemistry analysis of CD45 (A), F4/80 (B), CD4 (C) and CD8 (D) staining in WT, HET and PKN2 KO adenomas formed during the AOM/1%DSS protocol. **F)** PKN2 expression from RNA sequencing analysis in adenomas by genotype. Statistical significance was determined using DESeq2 differential expression analysis (WT: n=5, HET: n=10, KO: n=18). Adenomas from the same individuals are coloured with the same colours. **G)** Gene set enrichment analysis of KO vs WT, KO vs HET and HET vs WT adenomas for the most significant Hallmark gene sets. The top 15 most significant gene sets across all comparisons are shown. **H)** Gene set enrichment analysis of KO vs WT for colorectal Sansom APC and WNT, McMurray TP53/HRAS, Cordenonsi YAP, Berenjeno Q63L-RhoA and mouse phenotypes decreased tumour growth size gene sets.

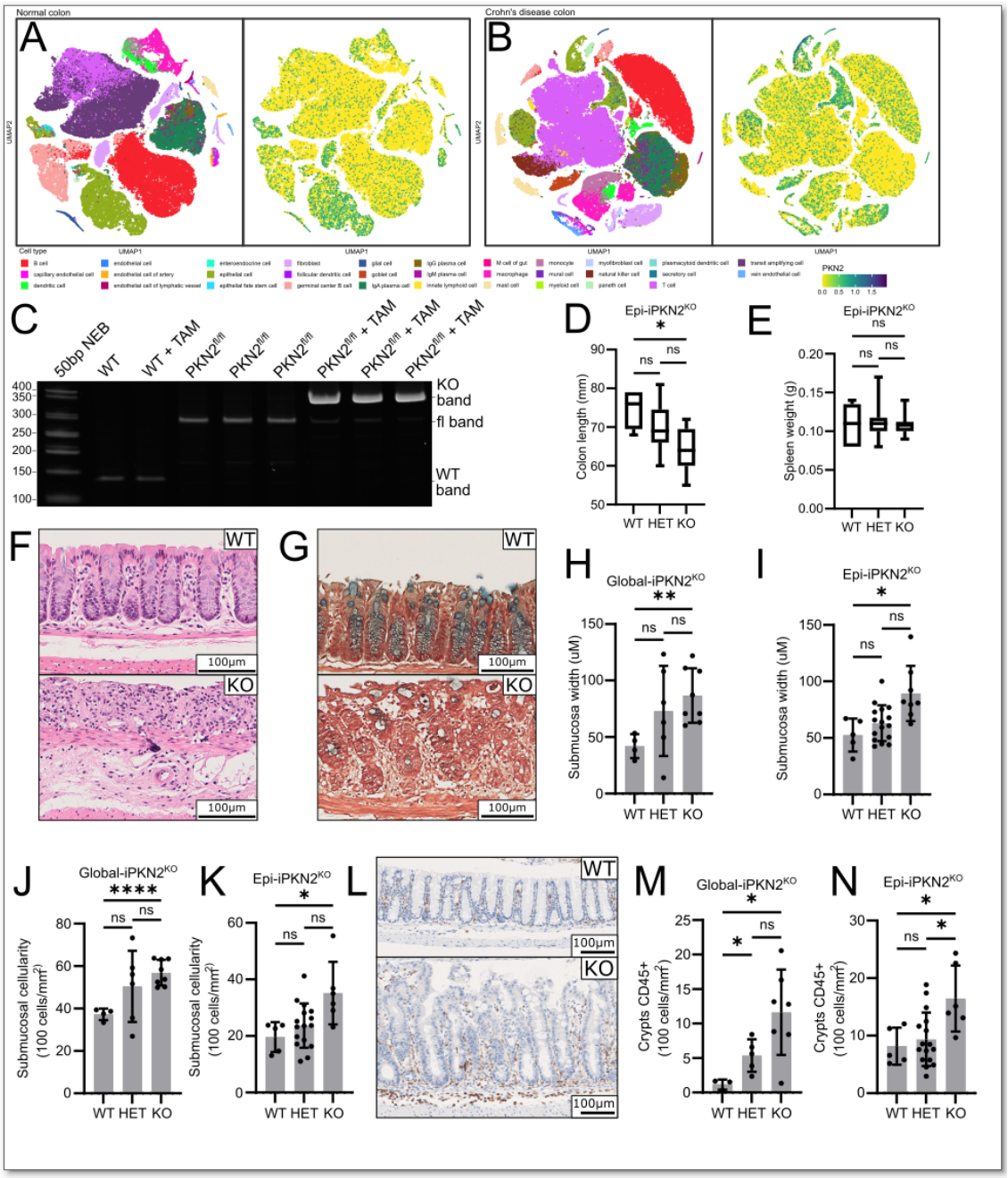

Figure S3: Epithelial specific PKN2 loss induces inflammatory damage. A, B) Single cell RNA sequencing analysis of samples from normal colon (A), Crohn's disease patients (B). Cell subtypes are coloured in the left panel with PKN2 expression labelled in the right panel. **C)** PCR genotyping of isolated colonic epithelial tissue two weeks following the tamoxifen treatment regime in Epi-iPKN2^{KO} mice. Diagram explaining band sizing is in Figure S1C. **D, E)** Colon length (D) and spleen weight (E) in Epi-iPKN2^{KO} mice following 5-days treatment with 2%DSS. Statistical significance was determined using a Dunnett's multiple comparisons test (WT: n=5, HET: n=16, KO: n=8). **F, G)** Epithelial erosion (F) and goblet cell depletion (G) indicated by alcian blue staining in Epi-iPKN2^{KO} mice following 5-days treatment with 2%DSS. **H-K)** Average distal submucosa width (H, I) and cellularity (J, K) in global-iPKN2KO (H, J) and Epi-PKN2KO (I, K) mice following treatment with AOM/1%DSS (H, J) or 2%DSS (I, K). Statistical significance was determined using a Dunnett's multiple comparisons test (H, J: WT: n= 4, HET: n=6, KO: n=8), (I, K: WT: n=5, HET: n=16, KO: n=8). **L-N)** CD45+ immune cell infiltration in distal crypts and submucosa global-iPKN2KO (N) and Epi-PKN2KO (L, N) mice following treatment with AOM/1%DSS (M) or 2%DSS (L, N). Statistical significance was determined using a Dunnett's multiple comparisons test (M: WT: n=3, HET: n=5, KO: n=7) (N: WT: n=5, HET: n=16, KO: n=6).

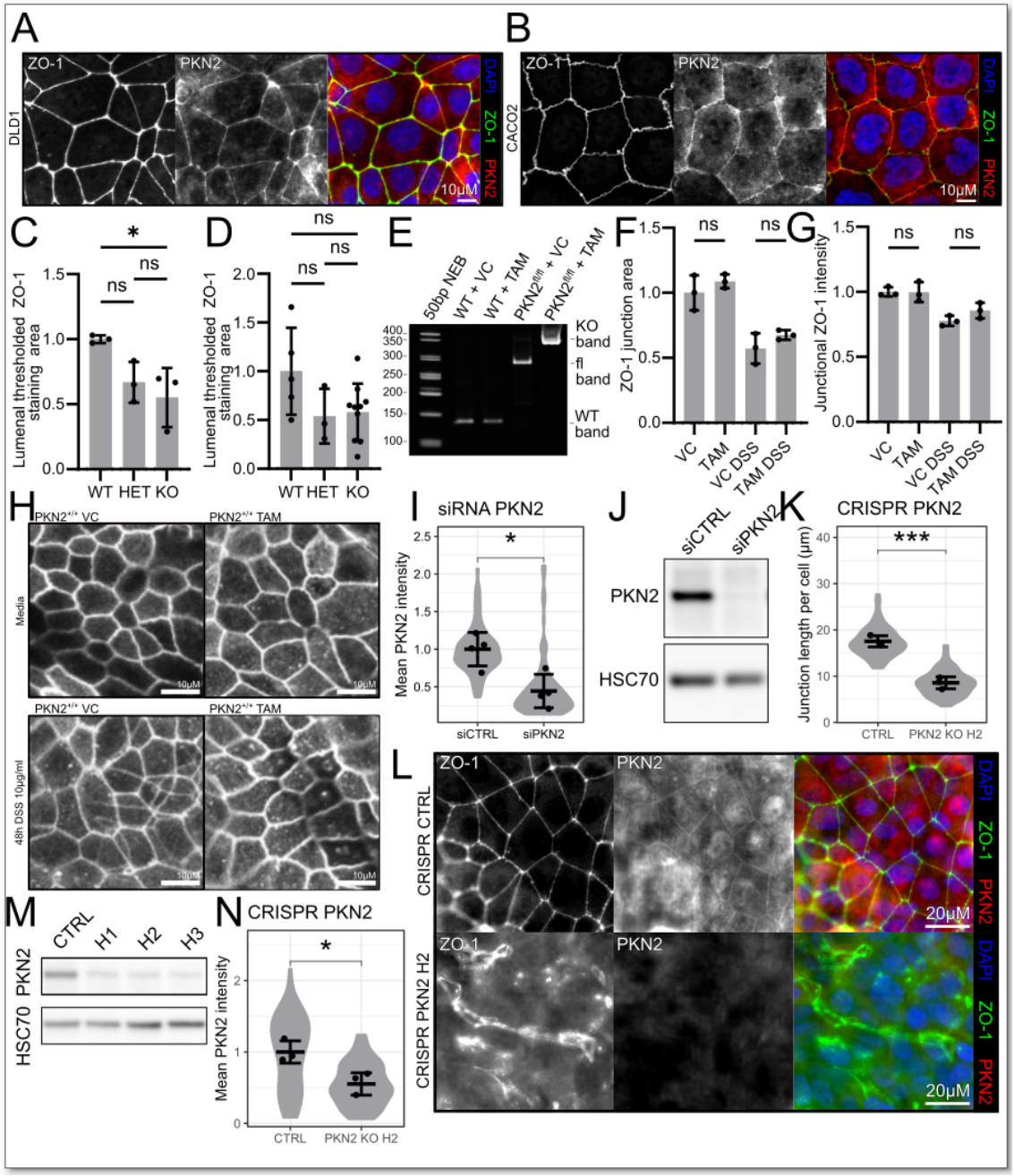

Figure S4: PKN2 regulates junctional ZO-1 integrity in cells, organoids, and mouse colon epithelium. A, B) Colocalization staining of junctional PKN2 and ZO-1 in DLD1 (A) and CACO2 (B) cells. **C, D)** Immunohistochemical analysis of distal colonic luminal epithelial ZO-1 staining in mice two weeks following PKN2 knockout induction (C) or 15 days following the initiation of 5 days of 1% DSS treatment (D). Statistical significance was determined using a Holm-Šídák's multiple comparisons test (C: n=9, D: n=18). **E)** PCR genotyping of colonic organoids one week following the in vitro tamoxifen treatment regime. Diagram explaining band sizing is in Figure S1B. **F-G)** Staining of ZO-1 in primary wild-type mouse organoids following 48h treatment with vehicle control or 48h 10µg/ml DSS. Graphs demonstrate a loss of junctional ZO-1 staining area (F) and intensity (G) following DSS treatment but no difference upon application of 4-OHT (TAM). Statistical significance was determined using a Holm-Šídák's multiple comparisons test (n=3). **I, J)** Loss of PKN2 protein

expression following PKN2 knockdown with a PKN2-targeting siRNA pool by immunofluorescence from stained junction images (I) and western blot analysis (J). Statistical significance was determined using an unpaired, two-tailed t-test (n=4). **K, L)** Loss of ZO-1 positive tight junction formation in a polyclonal DLD1 population following PKN2 knockout with CRISPR and selection. Tight junction loss was quantified by average length of junctional ZO-1 per cell. Statistical significance was determined using an unpaired, two-tailed t-test (n=3). **M, N)** Loss of PKN2 protein in three polyclonal DLD1 CRISPR cell lines by western blot (M) or just the H2 cell line by immunofluorescence (N). Statistical significance was determined using an unpaired, two-tailed t-test (n=3).

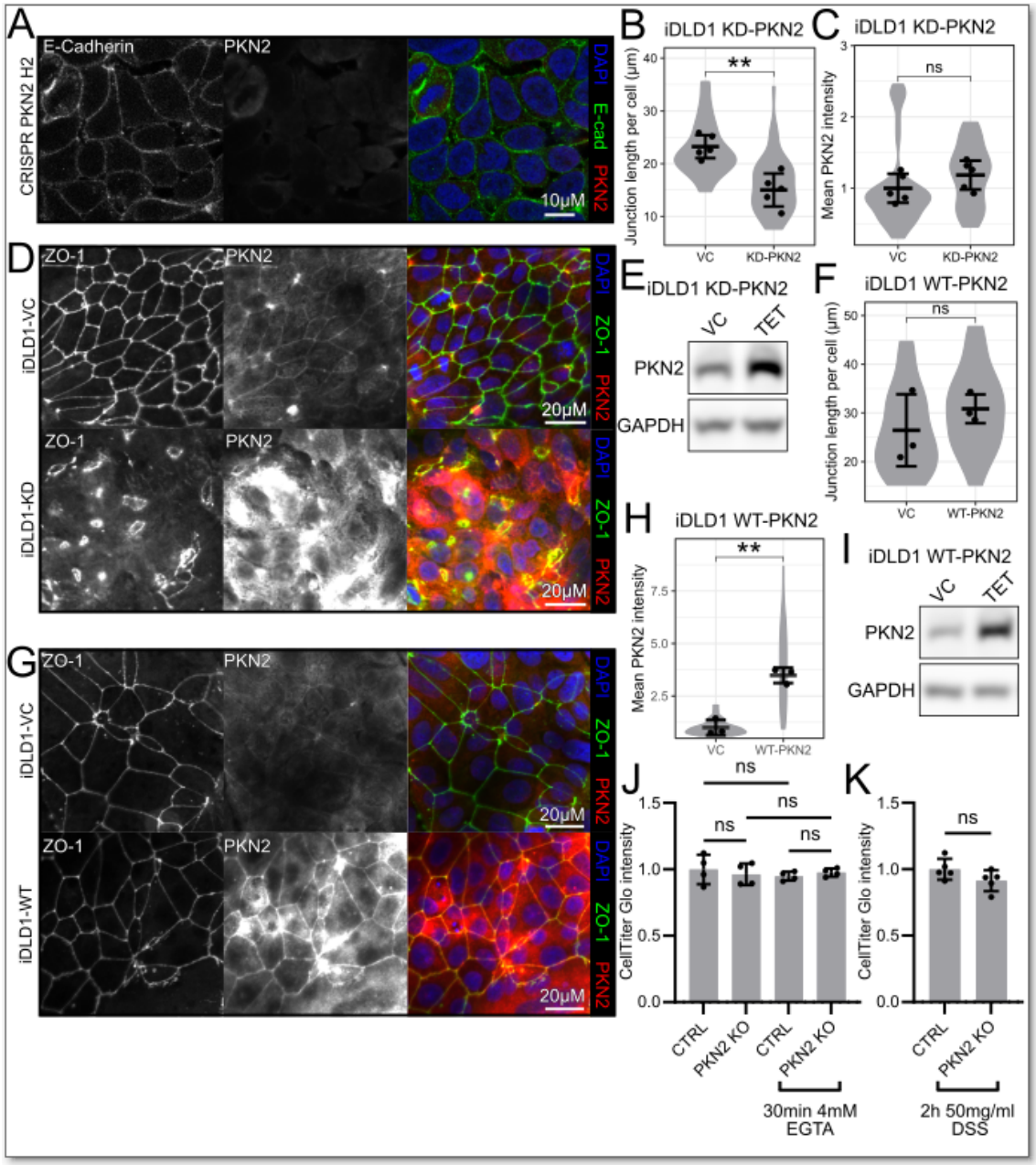

Figure S5: Impact of PKN2 knockout and overexpression on adherens and tight junctions. A) E-cadherin staining of adherens junctions in PKN2 knockout CRISPR cells. **B-E)** Loss of ZO1-positive tight junctions (A, D) and gain in PKN2 expression (C, D, E) following overexpression of a kinase-dead (KD)

PKN2 in the inducible DLD1 cell line (iDLD1). Statistical significance was determined using an unpaired, two-tailed t-test (n=5). **F-I)** Change in average junction length per cell (F, G) and gain in PKN2 expression (G, H, I) following overexpression of wild-type PKN2. Statistical significance was determined using an unpaired, two-tailed t-test (n=3). **J-K)** No statistically significant difference in CellTitre Glo intensity between CRISPR control and PKN2 KO gRNA lines following PKN2 KO, 4mM EGTA treatment (J) or 50mg/ml DSS (K). Statistical significance was determined using an unpaired, two-tailed t-test (J: n=4, K: n=5).

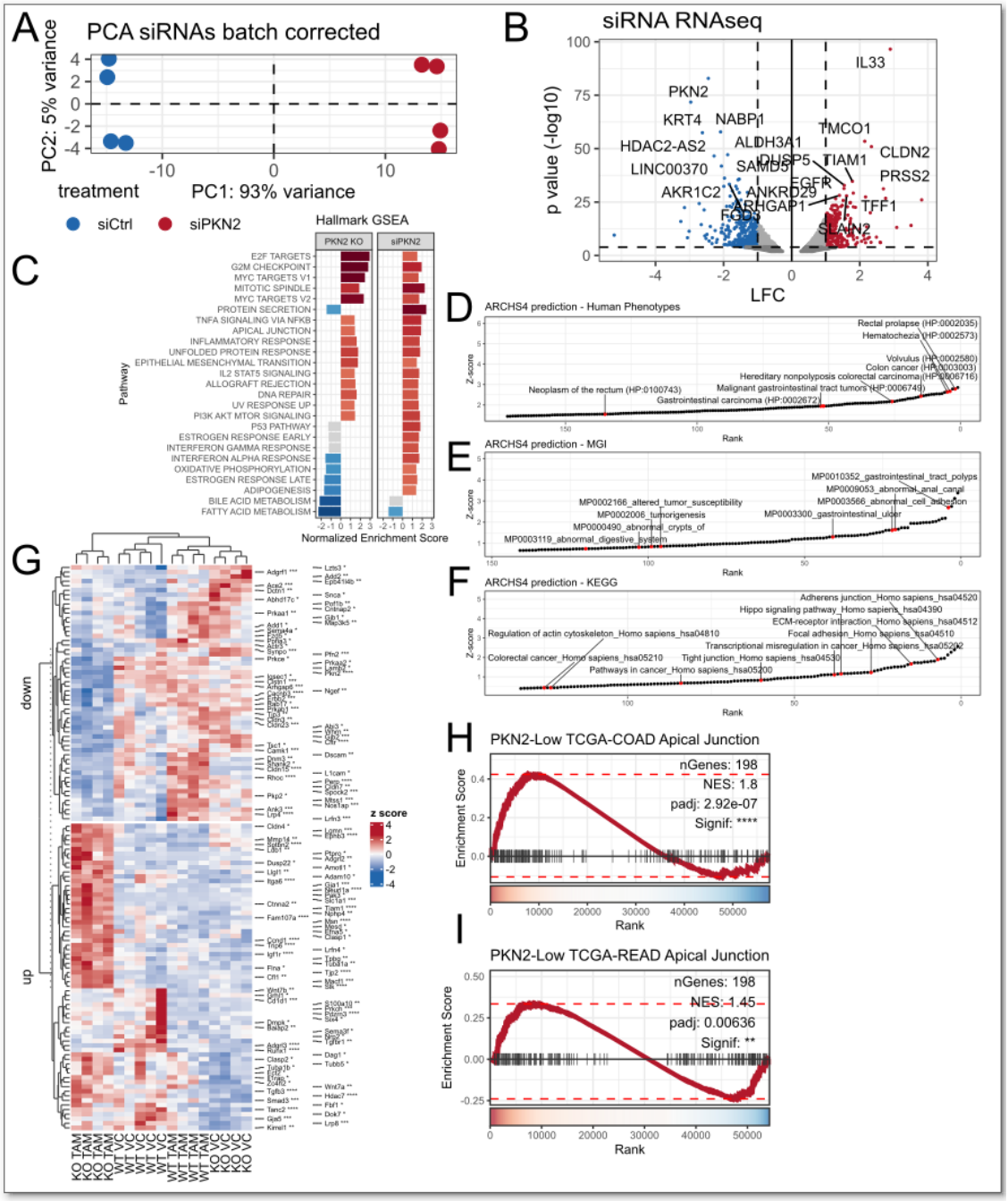

Figure S6: PKN2 loss alters gene expression, pathway enrichment, and junctional programs in cancer and colitis models. A) Principal component analysis of RNA sequencing data from DLD1 cells

treated with a PKN2 targeting siRNA or a non-targeting control. **B)** Differential gene expression analysis identifying the most significantly differentially expressed genes between DLD1 cells treated with a PKN2 targeting siRNA or a non-targeting control. **C)** Hallmark gene set enrichment analysis comparing the response of PKN2 KO in primary mouse organoids and DLD1 cancer cells treated with a PKN2-targeting siRNA. **D-F)** Predictions for PKN2 gene function from the ARCHS4 database containing massively integrated RNA sequencing data. Predictions are divided into human phenotypes (D), mouse genome informatics (MGI) (E) and Kyoto Encyclopedia of Genes and Genomes (KEGG) (F). **G)** Differential expression of cell junction genes in wild-type and Rosa$^{Cre/+}$/PKN2$^{fl/fl}$ mouse primary organoids treated with 4-OHT or a vehicle control. Differential expression significance stars are from a comparison between vehicle control and tamoxifen treated PKN2-KO organoids, accounting for the effects of tamoxifen treatment on wild-type organoids. **H, I)** GSEA of hallmark apical junction gene set in TCGA-COAD (H) and TCGA-READ (I) ranks created from comparing PKN2-low and PKN2-high patient primary tumours.

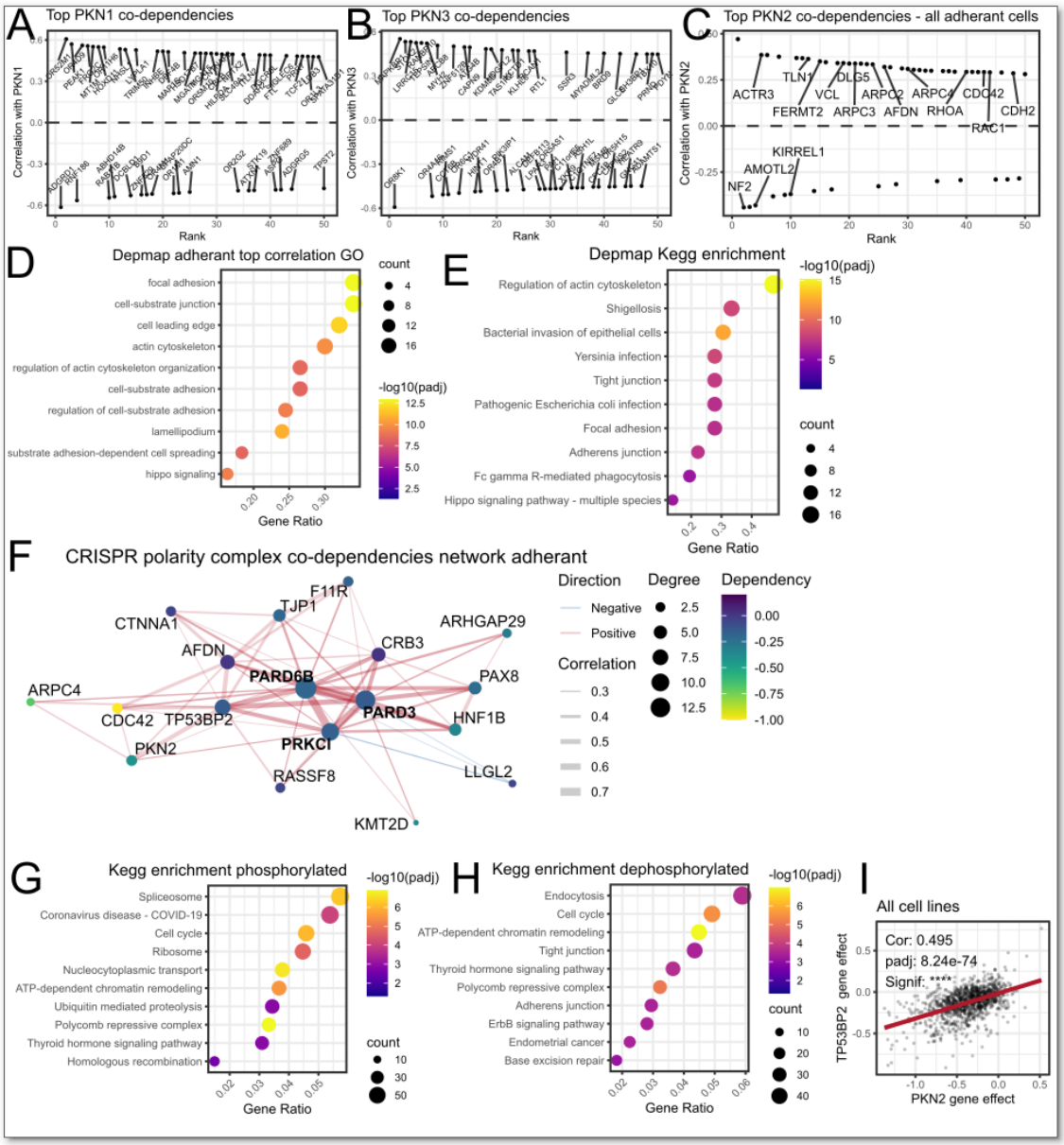

Figure S7: Co-dependency mapping of PKN family genes highlights junctional and Par complex networks. A, B) Top co-dependencies for PKN1 (A) and PKN3 (B) in bowel-linage cells from CRISPR screen data from the Cancer Dependency Map (DepMap) ranked by linear Pearson correlation coefficient. **C)** Top co-dependencies for PKN2 in all adherent cells from CRISPR screen data from the Cancer Dependency Map (DepMap) ranked by linear Pearson correlation coefficient. Genes in the GO:0034330 (cell junction organisation) and KEGG hsa04530 (tight junction) pathways are labelled. **D, E)** GO (D) and Kegg (E) term overrepresentation analysis on the top co-dependencies for PKN2 in all adherent cells as in C. **F)** Network analysis of the core Par complex genes PARD3, PARD6B and PRKCI highlighting their shared top co-dependencies in all adherent cells. Genes are represented as nodes and co-dependencies as edges. Nodes are sized by their degree and coloured by the genes mean individual dependency. Edge width corresponds with co-dependency strength between genes and coloured with direction. Network was assembled using the Fruchterman-Reingold layout algorithm. **G-H)** Overrepresentation analysis of phosphorylated (G) and dephosphorylated (H) proteins following overexpression of a de-regulated truncated PKN2 versus a kinase dead control in HEK293 cells using gene sets from the KEGG database. **I)** Relationship between gene dependency for PKN2 and TP53BP2 in all cell lines from the DepMap database.

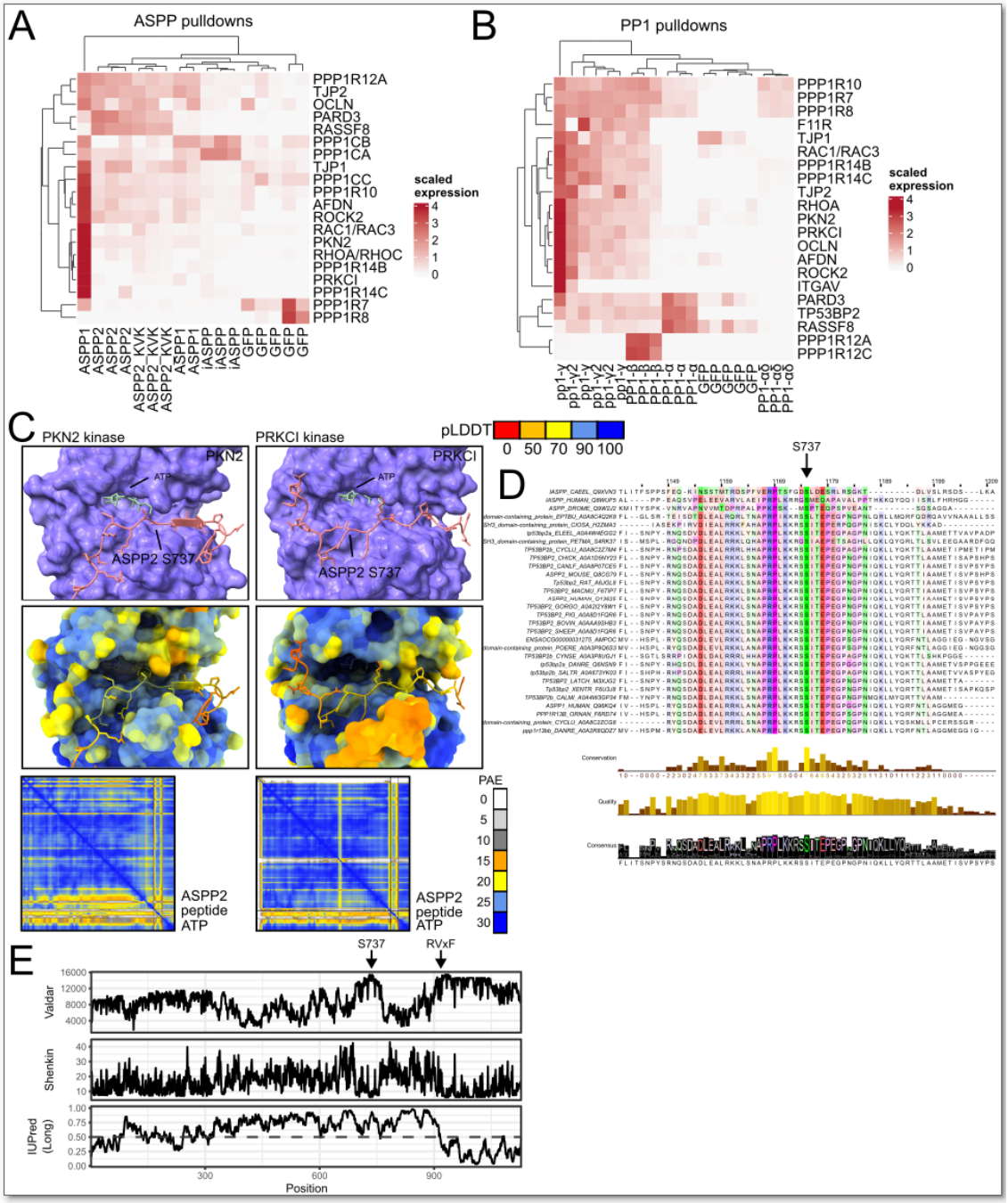

Figure S8: Protein interactions and structural conservation of the ASPP2 S737 region with PKN2 and PRKCI. A, B) Heatmaps of select proteins co-immunoprecipitated with ASPP family (A) and PP1 family (B) proteins in HEK293 cells obtained from PXD012378. **B)** AlphaFold multimer predictions of the S737 peptide in the cleft of the PKN2 and PRKCI kinase domains with ATP. Structures are coloured by chain in panel top, by predicted local distance difference test (pLDDT) panel centre and predicted aligned error (PAE) panel bottom. **C)** Conservation of the S737 region across 30 orthologues and paralogues of ASPP2 with alignment quality, consensus and Livingstone-barton conservation scores. **D)** Multi-sequence alignment of 30 orthologues and paralogues of ASPP2 annotated with IUPred intrinsically disordered region scores, Valdar and Shenkin conservation scores. IUPred scores above

0.5 are considered disordered. Conservation of S737 and RVxF regions are annotated with arrows. **E)** Conservation of the S737 region across 30 orthologues and paralogues of ASPP2 with alignment quality, consensus and Livingstone-barton conservation scores.

References

1 Ng, S. C. *et al.* Worldwide incidence and prevalence of inflammatory bowel disease in the 21st century: a systematic review of population-based studies. *Lancet* **390**, 2769-2778 (2017).

2 Ekbom, A., Helmick, C., Zack, M. & Adami, H. O. Ulcerative colitis and colorectal cancer. A population-based study. *N Engl J Med* **323**, 1228-1233 (1990).

3 Eaden, J. A., Abrams, K. R. & Mayberry, J. F. The risk of colorectal cancer in ulcerative colitis: a meta-analysis. *Gut* **48**, 526-535 (2001).

4 Gyde, S. N. *et al.* Colorectal cancer in ulcerative colitis: a cohort study of primary referrals from three centres. *Gut* **29**, 206-217 (1988).

5 Baron, J. A. *et al.* A randomized trial of aspirin to prevent colorectal adenomas. *N Engl J Med* **348**, 891-899 (2003).

6 Cole, B. F. *et al.* Aspirin for the chemoprevention of colorectal adenomas: meta-analysis of the randomized trials. *J Natl Cancer Inst* **101**, 256-266 (2009).

7 Bertagnolli, M. M. *et al.* Celecoxib for the prevention of sporadic colorectal adenomas. *N Engl J Med* **355**, 873-884 (2006).

8 Baron, J. A. *et al.* A randomized trial of rofecoxib for the chemoprevention of colorectal adenomas. *Gastroenterology* **131**, 1674-1682 (2006).

9 Jamieson, T. *et al.* Inhibition of CXCR2 profoundly suppresses inflammation-driven and spontaneous tumorigenesis. *J Clin Invest* **122**, 3127-3144 (2012).

10 Grivennikov, S. *et al.* IL-6 and Stat3 are required for survival of intestinal epithelial cells and development of colitis-associated cancer. *Cancer Cell* **15**, 103-113 (2009).

11 Putoczki, T. L. *et al.* Interleukin-11 is the dominant IL-6 family cytokine during gastrointestinal tumorigenesis and can be targeted therapeutically. *Cancer Cell* **24**, 257-271 (2013).

12 Greten, F. R. *et al.* IKKbeta links inflammation and tumorigenesis in a mouse model of colitis-associated cancer. *Cell* **118**, 285-296 (2004).

13 Cho, J. H. *et al.* Identification of novel susceptibility loci for inflammatory bowel disease on chromosomes 1p, 3q, and 4q: evidence for epistasis between 1p and IBD1. *Proc Natl Acad Sci U S A* **95**, 7502-7507 (1998).

14 Cho, J. H. *et al.* Linkage and linkage disequilibrium in chromosome band 1p36 in American Chaldeans with inflammatory bowel disease. *Hum Mol Genet* **9**, 1425-1432 (2000).

15 El Hadad, J., Schreiner, P., Vavricka, S. R. & Greuter, T. The Genetics of Inflammatory Bowel Disease. *Mol Diagn Ther* **28**, 27-35 (2024).

16 Ermann, J. *et al.* Severity of innate immune-mediated colitis is controlled by the cytokine deficiency-induced colitis susceptibility-1 (Cdcs1) locus. *Proc Natl Acad Sci U S A* **108**, 7137-7141 (2011).

17 Mahler, M. *et al.* Genetics of colitis susceptibility in IL-10-deficient mice: backcross versus F2 results contrasted by principal component analysis. *Genomics* **80**, 274-282 (2002).

18 Farmer, M. A. *et al.* A major quantitative trait locus on chromosome 3 controls colitis severity in IL-10-deficient mice. *Proc Natl Acad Sci U S A* **98**, 13820-13825 (2001).

19 Borm, M. E. *et al.* A major quantitative trait locus on mouse chromosome 3 is involved in disease susceptibility in different colitis models. *Gastroenterology* **128**, 74-85 (2005).

20 Meunier, C. *et al.* Characterization of a major colon cancer susceptibility locus (Ccs3) on mouse chromosome 3. *Oncogene* **29**, 647-661 (2010).

21 Quetier, I. *et al.* Knockout of the PKN Family of Rho Effector Kinases Reveals a Non-redundant Role for PKN2 in Developmental Mesoderm Expansion. *Cell Rep* **14**, 440-448 (2016).

22 Murray, E. R. *et al.* Disruption of pancreatic stellate cell myofibroblast phenotype promotes pancreatic tumor invasion. *Cell Rep* **38**, 110227 (2022).
23 De Robertis, M. *et al.* The AOM/DSS murine model for the study of colon carcinogenesis: From pathways to diagnosis and therapy studies. *J Carcinog* **10**, 9 (2011).
24 Cooper, H. S., Murthy, S. N., Shah, R. S. & Sedergran, D. J. Clinicopathologic study of dextran sulfate sodium experimental murine colitis. *Lab Invest* **69**, 238-249 (1993).
25 Foley, J. W. *et al.* Gene expression profiling of single cells from archival tissue with laser-capture microdissection and Smart-3SEQ. *Genome Res* **29**, 1816-1825 (2019).
26 Berenjeno, I. M., Nunez, F. & Bustelo, X. R. Transcriptomal profiling of the cellular transformation induced by Rho subfamily GTPases. *Oncogene* **26**, 4295-4305 (2007).
27 Wallace, S. W., Magalhaes, A. & Hall, A. The Rho target PRK2 regulates apical junction formation in human bronchial epithelial cells. *Molecular and cellular biology* **31**, 81-91 (2011).
28 Tan, B. *et al.* The Mammalian Crumbs Complex Defines a Distinct Polarity Domain Apical of Epithelial Tight Junctions. *Curr Biol* **30**, 2791-2804 e2796 (2020).
29 Poritz, L. S. *et al.* Loss of the tight junction protein ZO-1 in dextran sulfate sodium induced colitis. *J Surg Res* **140**, 12-19 (2007).
30 Paradis, T., Begue, H., Basmaciyan, L., Dalle, F. & Bon, F. Tight Junctions as a Key for Pathogens Invasion in Intestinal Epithelial Cells. *Int J Mol Sci* **22** (2021).
31 Sarvestani, S. K. *et al.* Cancer-predicting transcriptomic and epigenetic signatures revealed for ulcerative colitis in patient-derived epithelial organoids. *Oncotarget* **9**, 28717-28730 (2018).
32 Pan, J. *et al.* Interrogation of Mammalian Protein Complex Structure, Function, and Membership Using Genome-Scale Fitness Screens. *Cell Syst* **6**, 555-568 e557 (2018).
33 Killarney, S. T. *et al.* PKN2 Is a Dependency of the Mesenchymal-like Cancer Cell State. *Cancer Discov* **15**, 595-615 (2025).
34 Oughtred, R. *et al.* The BioGRID database: A comprehensive biomedical resource of curated protein, genetic, and chemical interactions. *Protein Sci* **30**, 187-200 (2021).
35 Go, C. D. *et al.* A proximity-dependent biotinylation map of a human cell. *Nature* **595**, 120-124 (2021).
36 Amano, M. *et al.* A proteomic approach for comprehensively screening substrates of protein kinases such as Rho-kinase. *PloS one* **5**, e8704 (2010).
37 Horikoshi, Y. *et al.* Interaction between PAR-3 and the aPKC-PAR-6 complex is indispensable for apical domain development of epithelial cells. *J Cell Sci* **122**, 1595-1606 (2009).
38 Benton, R. & St Johnston, D. Drosophila PAR-1 and 14-3-3 inhibit Bazooka/PAR-3 to establish complementary cortical domains in polarized cells. *Cell* **115**, 691-704 (2003).
39 Calcagno, S. R. *et al.* Protein kinase C iota in the intestinal epithelium protects against dextran sodium sulfate-induced colitis. *Inflamm Bowel Dis* **17**, 1685-1697 (2011).
40 Langton, P. F. *et al.* The dASPP-dRASSF8 complex regulates cell-cell adhesion during Drosophila retinal morphogenesis. *Curr Biol* **19**, 1969-1978 (2009).
41 Cong, W. *et al.* ASPP2 regulates epithelial cell polarity through the PAR complex. *Curr Biol* **20**, 1408-1414 (2010).
42 Sottocornola, R. *et al.* ASPP2 binds Par-3 and controls the polarity and proliferation of neural progenitors during CNS development. *Dev Cell* **19**, 126-137 (2010).
43 Bertran, M. T. *et al.* ASPP proteins discriminate between PP1 catalytic subunits through their SH3 domain and the PP1 C-tail. *Nat Commun* **10**, 771 (2019).
44 Yamashita, K. *et al.* Phosphorylation and dephosphorylation of Ser852 and Ser889 control the clustering, localization and function of PAR3. *J Cell Sci* **133** (2020).
45 Beutel, O., Maraspini, R., Pombo-Garcia, K., Martin-Lemaitre, C. & Honigmann, A. Phase Separation of Zonula Occludens Proteins Drives Formation of Tight Junctions. *Cell* **179**, 923-936 e911 (2019).

46 Sun, D. *et al.* Assembly of tight junction belts by ZO1 surface condensation and local actin polymerization. *Dev Cell* **60**, 1234-1250 e1236 (2025).
47 Piovesan, D. *et al.* MobiDB: 10 years of intrinsically disordered proteins. *Nucleic Acids Res* **51**, D438-D444 (2023).
48 Konya, Z. *et al.* Phosphorylated Peptide Derived from the Myosin Phosphatase Target Subunit Is a Novel Inhibitor of Protein Phosphatase-1. *Int J Mol Sci* **24** (2023).
49 Filter, J. J., Williams, B. C., Eto, M., Shalloway, D. & Goldberg, M. L. Unfair competition governs the interaction of pCPI-17 with myosin phosphatase (PP1-MYPT1). *Elife* **6** (2017).
50 Lemaire, S. & Bollen, M. Protein phosphatase-1: dual activity regulation by Inhibitor-2. *Biochem Soc Trans* **48**, 2229-2240 (2020).
51 Terrak, M., Kerff, F., Langsetmo, K., Tao, T. & Dominguez, R. Structural basis of protein phosphatase 1 regulation. *Nature* **429**, 780-784 (2004).
52 Saitou, M. *et al.* Complex phenotype of mice lacking occludin, a component of tight junction strands. *Mol Biol Cell* **11**, 4131-4142 (2000).
53 Schulzke, J. D. *et al.* Epithelial transport and barrier function in occludin-deficient mice. *Biochim Biophys Acta* **1669**, 34-42 (2005).
54 Khounlotham, M. *et al.* Compromised intestinal epithelial barrier induces adaptive immune compensation that protects from colitis. *Immunity* **37**, 563-573 (2012).
55 Laukoetter, M. G. *et al.* JAM-A regulates permeability and inflammation in the intestine in vivo. *J Exp Med* **204**, 3067-3076 (2007).
56 Kuo, W. T. *et al.* The Tight Junction Protein ZO-1 Is Dispensable for Barrier Function but Critical for Effective Mucosal Repair. *Gastroenterology* **161**, 1924-1939 (2021).
57 Van der Hoeven, G. *et al.* Spontaneous and chaperone-assisted metal loading in the active site of protein phosphatase-1. *FEBS Lett* **598**, 2876-2885 (2024).
58 Hamaguchi, T. *et al.* Phosphorylation of CPI-17, an inhibitor of myosin phosphatase, by protein kinase N. *Biochem Biophys Res Commun* **274**, 825-830 (2000).
59 Davies, S. P., Reddy, H., Caivano, M. & Cohen, P. Specificity and mechanism of action of some commonly used protein kinase inhibitors. *Biochem J* **351**, 95-105 (2000).
60 Nishioka, T., Nakayama, M., Amano, M. & Kaibuchi, K. Proteomic screening for Rho-kinase substrates by combining kinase and phosphatase inhibitors with 14-3-3zeta affinity chromatography. *Cell Struct Funct* **37**, 39-48 (2012).
61 Amieva, M. R. *et al.* Disruption of the epithelial apical-junctional complex by Helicobacter pylori CagA. *Science* **300**, 1430-1434 (2003).
62 Buti, L. *et al.* CagA-ASPP2 complex mediates loss of cell polarity and favors H. pylori colonization of human gastric organoids. *Proc Natl Acad Sci U S A* **117**, 2645-2655 (2020).
63 Nesic, D., Buti, L., Lu, X. & Stebbins, C. E. Structure of the Helicobacter pylori CagA oncoprotein bound to the human tumor suppressor ASPP2. *Proc Natl Acad Sci U S A* **111**, 1562-1567 (2014).
64 Mishra, J. P. *et al.* CagA of Helicobacter pylori interacts with and inhibits the serine-threonine kinase PRK2. *Cell Microbiol* **17**, 1670-1682 (2015).
65 Divaris, K. *et al.* Genome-wide association study of periodontal pathogen colonization. *J Dent Res* **91**, 21S-28S (2012).
66 Arafeh, R., Shibue, T., Dempster, J. M., Hahn, W. C. & Vazquez, F. The present and future of the Cancer Dependency Map. *Nat Rev Cancer* **25**, 59-73 (2025).
67 Wu, F. *et al.* Genome-wide gene expression differences in Crohn's disease and ulcerative colitis from endoscopic pinch biopsies: insights into distinctive pathogenesis. *Inflamm Bowel Dis* **13**, 807-821 (2007).
68 van Wezel, T., Ruivenkamp, C. A., Stassen, A. P., Moen, C. J. & Demant, P. Four new colon cancer susceptibility loci, Scc6 to Scc9 in the mouse. *Cancer Res* **59**, 4216-4218 (1999).
69 Moolenbeek, C. & Ruitenberg, E. J. The "Swiss roll": a simple technique for histological studies of the rodent intestine. *Lab Anim* **15**, 57-59 (1981).

70 Bankhead, P. *et al.* QuPath: Open source software for digital pathology image analysis. *Sci Rep* **7**, 16878 (2017).
71 Qin, X. *et al.* Cell-type-specific signaling networks in heterocellular organoids. *Nat Methods* **17**, 335-342 (2020).
72 Takahashi, Y. *et al.* A Refined Culture System for Human Induced Pluripotent Stem Cell-Derived Intestinal Epithelial Organoids. *Stem Cell Reports* **10**, 314-328 (2018).
73 Doench, J. G. *et al.* Optimized sgRNA design to maximize activity and minimize off-target effects of CRISPR-Cas9. *Nat Biotechnol* **34**, 184-191 (2016).
74 Giuliano, C. J., Lin, A., Girish, V. & Sheltzer, J. M. Generating Single Cell-Derived Knockout Clones in Mammalian Cells with CRISPR/Cas9. *Curr Protoc Mol Biol* **128**, e100 (2019).
75 Carpenter, A. E. *et al.* CellProfiler: image analysis software for identifying and quantifying cell phenotypes. *Genome Biol* **7**, R100 (2006).
76 Hornbeck, P. V. *et al.* PhosphoSitePlus, 2014: mutations, PTMs and recalibrations. *Nucleic Acids Res* **43**, D512-520 (2015).
77 UniProt, C. UniProt: the Universal Protein Knowledgebase in 2025. *Nucleic Acids Res* **53**, D609-D617 (2025).
78 Shiga, K. *et al.* Development of an intracellularly acting inhibitory peptide selective for PKN. *Biochem J* **425**, 445-453 (2009).
79 Passman, A. M. *et al.* Hepatocytes undergo punctuated expansion dynamics from a periportal stem cell niche in normal human liver. *J Hepatol* **79**, 417-432 (2023).
80 Love, M. I., Huber, W. & Anders, S. Moderated estimation of fold change and dispersion for RNA-seq data with DESeq2. *Genome Biol* **15**, 550 (2014).
81 Korotkevich, G., Sukhov, V. & Sergushichev, A. Fast gene set enrichment analysis. *bioRxiv* (2019).
82 Subramanian, A. *et al.* Gene set enrichment analysis: a knowledge-based approach for interpreting genome-wide expression profiles. *Proc Natl Acad Sci U S A* **102**, 15545-15550 (2005).
83 Wickham, H. in *Use R!,* 1 online resource (XVI, 260 pages 232 illustrations, 140 illustrations in color (Springer International Publishing : Imprint: Springer,, Cham, 2016).
84 Gu, Z., Eils, R. & Schlesner, M. Complex heatmaps reveal patterns and correlations in multidimensional genomic data. *Bioinformatics* **32**, 2847-2849 (2016).
85 Haberman, Y. *et al.* Pediatric Crohn disease patients exhibit specific ileal transcriptome and microbiome signature. *J Clin Invest* **124**, 3617-3633 (2014).
86 Kong, L. *et al.* The landscape of immune dysregulation in Crohn's disease revealed through single-cell transcriptomic profiling in the ileum and colon. *Immunity* **56**, 444-458 e445 (2023).
87 Smillie, C. S. *et al.* Intra- and Inter-cellular Rewiring of the Human Colon during Ulcerative Colitis. *Cell* **178**, 714-730 e722 (2019).
88 Pelka, K. *et al.* Spatially organized multicellular immune hubs in human colorectal cancer. *Cell* **184**, 4734-4752 e4720 (2021).
89 Lachmann, A. *et al.* PrismEXP: gene annotation prediction from stratified gene-gene co-expression matrices. *PeerJ* **11**, e14927 (2023).